RESEARCH ARTICLE



Modification of a Wavelet-Based Method for Detecting Ebullitive Methane Fluxes in Eddy-Covariance Observations: Application at Two Rice Fields

Will P. Richardson¹ • Michele L. Reba² • Benjamin R. K. Runkle¹

Received: 18 October 2021 / Accepted: 21 March 2022 / Published online: 30 April 2022 © The Author(s), under exclusive licence to Springer Nature B.V. 2022

Abstract

Ebullition, the release of gas bubbles, is an important pathway of methane emission in many ecosystems, yet its high spatio-temporal variability makes it challenging to quantify. In this work, a methane-flux partitioning method based on scalar similarity in the wavelet domain is applied to eddy-covariance data collected at two flooded rice fields. Inspection of initial results indicates that several modifications are needed for robust ebullition detection. With these modifications, our objectives are to compare the original and modified methods, conduct a sensitivity analysis of the program's empirical parameters, characterize the importance of ebullition in rice across growth stages, and identify the primary drivers of ebullition. The modified method's ebullitive fluxes are significantly lower and show lower variance than those from the original method. Furthermore, the two methods produce distinct patterns of diel variation. While partitioning estimates show non-trivial sensitivity to the program parameters, this sensitivity is lower in magnitude than the random error in the ebullitive flux estimates. Ebullitive fluxes make up 9% of the total flux on average, with ebullition increasing in importance as plants develop. Ebullitive fluxes are best predicted by wind speed (negative effect), ecosystem respiration (positive effect), and sensible heat flux (positive effect), suggesting an indirect effect of plant-mediated transport, a link with temperature and methane production, and a potential effect of water column turnover, respectively. In addition to validating the method with independent ebullition observations, we recommend its application at more natural and managed wetlands to improve understanding of this highly variable transport pathway.

 $\label{lem:keywords} \textbf{Keywords} \ \ Ebullition \cdot Flux \ partitioning \cdot Land-atmosphere \ interactions \cdot Scalar \\ similarity \cdot Wetlands$

United States Department of Agriculture – Agricultural Research Service, Delta Water Management Research Unit, Jonesboro, AR 72401, USA



Will P. Richardson wprichar@uark.edu

Department of Biological and Agricultural Engineering, University of Arkansas, Fayetteville, AR 72701, USA

1 Introduction

Methane (CH₄) is a potent greenhouse gas with a global warming potential 80 times that of carbon dioxide (CO₂) over a 20-year time horizon (Forster et al. 2021). Due to the relatively short lifetime of CH₄ in the atmosphere, changes in emissions can significantly alter the amount of warming that occurs in the near future (United Nations Environment Programme & Climate and Clean Air Coalition 2021), making improved monitoring of CH₄ emissions critical for predicting future warming trends. Of total global CH₄ emissions, roughly 25% are contributed by wetlands (20%) and rice agriculture (5%, or 8% of anthropogenic CH₄ emissions), with wetlands also being one of the most important sources of uncertainty in the CH₄ budget (Saunois et al. 2020). Thus, further study of the processes involved in CH₄ emission from these systems has the potential both to constrain their current contributions to the CH₄ budget and aid in understanding how they may change in future climate scenarios.

A key part of quantifying the CH₄ emissions from rice fields and other wetland ecosystems is determining the contribution of different emission pathways to the total CH4 flux. These systems emit CH₄ via three main pathways: plant-mediated transport through aerenchyma tissue, diffusion from the water column, and ebullition through the soil-water matrix (i.e., the release of gas bubbles enriched in CH₄) (Wassmann and Aulakh 2000; Le Mer and Roger 2001), each having unique biophysical controls. Of these pathways, ebullition is particularly challenging to characterize due to its high spatiotemporal variability (Comas and Wright 2012; Wik et al. 2016), and its relative contribution to the total CH₄ flux can vary widely across ecosystem type and within different periods of the growing season (≈2–90%; Butterbach-Bahl et al. 1997; Tokida et al. 2007; Santoni et al. 2012; Stamp et al. 2013; Hoffmann et al. 2017; McNicol et al. 2017; Männistö et al. 2019; Stanley et al. 2019; Villa et al. 2021). Therefore, accurate estimates of CH₄ ebullition fluxes and their relative contribution to total CH₄ fluxes are critically needed to improve our understanding of biophysical controls on CH₄ flux partitioning, improve model-based estimates of net CH₄ fluxes, and accurately predict changes in CH₄ emissions under future climate scenarios (Riley et al. 2011; Xu et al. 2016). The recent projection that ebullitive, not diffusive, CH₄ fluxes will increase due to climate change (6–20% per 1°C increase; Aben et al. 2017) further underscores the need for improved representation of CH₄ emission processes in models to accurately characterize future climate feedbacks.

However, estimates of ebullition remain relatively scarce, in part because a direct estimate of ebullition typically requires highly replicated manual observations using bubble traps or similar small chambers (Wassmann et al. 1996; Wik et al. 2013; McNicol et al. 2017; Wang et al. 2021). Commonly used techniques for measuring total CH₄ fluxes such as the eddy-covariance method do not explicitly distinguish between emission pathways (Morin et al. 2014; Knox et al. 2016). While eddy-covariance systems should capture sporadic ebullitive fluxes due to their high temporal resolution, quasi-continuous observation, and relatively large sampling areas, conventional data processing protocols estimate the net CH₄ flux. Fortunately, recent studies have shown that ebullition is typically associated with sudden, sharp fluctuations in CH₄ concentration, which leave distinct patterns in the resulting time series (Komiya et al. 2015; Hoffmann et al. 2017; Iwata et al. 2018).

While measurements of CH₄ concentration alone would not be sufficient to identify ebullition in atmospheric turbulence measurements, concurrent observations of other routinely measured atmospheric scalars such as H₂O, CO₂, and temperature can be used to isolate the sporadic CH₄ fluctuations associated with ebullition. When making measurements over



homogeneous terrain, the sources and sinks of these scalars are uniformly distributed, leading to similar turbulent fluctuations between gases, or scalar similarity (Monin and Obukhov 1954; Katul et al. 1995). Iwata et al. (2018) showed that ebullition violated this scalar similarity, and they subsequently developed a method for partitioning eddy-covariance CH₄ fluxes from a shallow lake into ebullitive and diffusive components by assessing the similarity between CH₄ and reference scalar fluctuations in the wavelet domain. Because this method only requires some empirical parameters and basic site information such as measurement height, it can readily be applied to any set of eddy-covariance observations, provided that the raw high-frequency data are available. Thus it has the potential to vastly improve our understanding of CH₄ ebullition across many site-years of observations from networks of long-term eddy-covariance stations (e.g., FLUXNET-CH4, Knox et al. 2019; Delwiche et al. 2021). However, the method has only been applied twice since its development: Taoka et al. (2020) conducted a year-long study on dynamics of flux partitioning and their environmental controls at the site where the method was developed, and Hwang et al. (2020) used the method in an assessment of carbon dynamics across three growing seasons in a rice paddy. Implementing this CH₄ flux-partitioning method at more sites is critical for confirming its accuracy across a range of landscape types and measurement conditions (e.g., differences in observation height, canopy height, reference scalar flux magnitudes, etc.). Furthermore, Iwata et al. (2018) showed that the partitioning results were sensitive to one of the aforementioned empirical parameters, suggesting the need for more sensitivity analyses and methodological interrogation to improve the method's robustness.

In this study we apply the CH₄ flux-partitioning method of Iwata et al. (2018) to eddy-covariance observations from two adjacent rice fields under delayed flood irrigation. Upon implementing the partitioning method, we found that several modifications were necessary for the method to consistently and correctly isolate the ebullitive component of CH₄ fluxes across the growing season. Thus, the first objective is to document and test the modifications we made to the method, describe the physical basis for their role in improving the accuracy of ebullition estimates, and present example 30-min periods demonstrating their effects on the method's performance. Due to the inherently empirical nature of the method, our second objective is to conduct a sensitivity analysis by running the partitioning program using a range of possible parameter sets for our site. This sensitivity analysis will inform our selection of a 'finalized' set of parameters in the absence of further ground-based validation of the method. With these 'best' ebullitive flux estimates and their associated uncertainty, our last objective is to characterize the importance of ebullition across different stages of crop development and identify the main biophysical drivers of ebullition.

2 Methods

2.1 Site Description

The study dataset was collected during the 2017 growing season at two adjacent, commercially farmed rice fields in Lonoke County, Arkansas, USA [34.58551° N, 91.75167° W; humid subtropical climate with hot summers (Cfa, Kottek et al. 2006); see Fig. 1 in Runkle et al. 2019]. Both fields span approximately 26 ha (350 m by 750 m), were zero-grade levelled in 2006, and have since been under continuous single-crop rice production. Despite their close proximity, the two fields have slight differences in soil texture and properties (e.g., clay content, organic matter, etc.). Both fields were drill-seed planted with XL745 hybrid



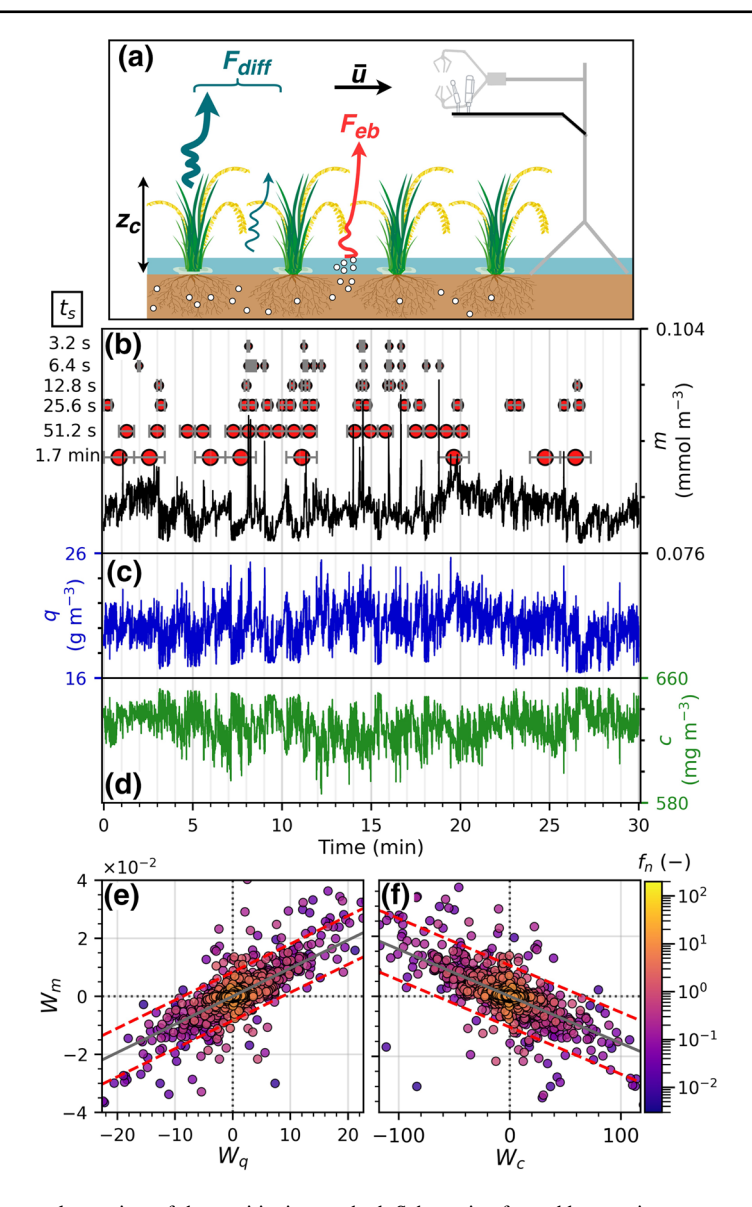


Fig. 1 Conceptual overview of the partitioning method. Schematic of an eddy-covariance system observing diffusive (F_{diff}) and ebullitive (F_{eb}) fluxes from an inundated rice field ($\bf a$, where z_c is canopy height and $\bar a$ is the mean wind speed during observation); time series of methane (m), water vapour (q), and carbon dioxide (c) concentrations ($\bf b$, $\bf c$, and $\bf d$, respectively) during a period with substantial ebullition (3 August 1600 LT, local time = UTC – 5 h); wavelet coefficient scatterplots used to assess scalar similarity by comparing methane coefficients (W_m) with those of two reference scalars, water vapour (W_q), and carbon dioxide (W_c) ($\bf e$ and $\bf f$, respectively). Points in $\bf e$ and $\bf f$ are coloured by their normalized frequency (f_n) values, and the dashed red lines are the bounds of the ebullition threshold (i.e., points not contained by the lines are considered to be the result of ebullition). The time locations of ebullitive wavelet coefficients spanning time scales (t_s) \approx 3.2 s–1.7 min have been plotted in red above the methane time series in $\bf b$; see Eqs. 3 and 5 for more information on formulation of f_n and its relationship to t_s



seed (Rice Tec., Alvin, Texas); the north field was planted on 10 April and harvested on 26 August, and the south field was planted on 9 April and harvested on 27 August. Monthly mean temperatures ranged from 18.8 to 27.8 °C, and cumulative rainfall during the study period was 868 mm, substantially wetter than normal (492 mm). Both fields were treated with urea and diammonium phosphate (DAP) fertilizers (155 kg urea-N ha⁻¹ in 3 doses, 20 kg DAP-N ha⁻¹ in 1 dose) and managed with the delayed flood irrigation practice, through which the field is inundated from the five-leaf stage until just before harvest. For additional details on site characteristics, management practices, and yields, see Runkle et al. (2019) and Suvočarev et al. (2019).

2.2 Flux and Ancillary Data

Fluxes of CH₄, CO₂, H₂O, and sensible heat (*H*) were measured using the eddy-covariance technique. Both fields were monitored with identical measurement systems consisting of a three-dimensional sonic anemometer (CSAT3, Campbell Scientific, Inc., Logan, Utah, U.S.A.), an open-path CO₂ and H₂O infrared gas analyzer (LI-7500A, LI-COR Inc., Lincoln, Nebraska, U.S.A.) and an open-path CH₄ analyzer (LI-7700, LI-COR Inc.). Instruments were mounted on a tower at 2.28 m (north field; US-HRC) and 2.26 m (south field; US-HRA) above the ground. The towers were positioned at the north edge of each field in order to ensure adequate fetch, as winds at the site predominantly come from the south. Instruments were installed 3 days after planting and remained installed until 3 days before harvest. High frequency wind speed and gas concentration measurements were recorded at 20 Hz through an Analyzer Interface Unit (LI-7550, LI-COR Inc.) with the LI-COR SMARTflux automated processing system. Station outages prevented data collection from 20 April to 18 May at the north field as well as from 18 to 25 April and 23 May to 9 June at the south field.

EddyPro software (v. 7.0.6, LI-COR Inc., Lincoln, NE, U.S.A.) was used for processing the raw high-frequency data, calculation of 30-min turbulent fluxes (with the exception of CH₄ fluxes; see Sect. 2.3.2), and quality control of fluxes. Wind vector measurements from the sonic anemometer were first corrected for transducer shadowing (Horst et al. 2015), and then coordinates were transformed using a double rotation. All high-frequency data were put through a series of statistical tests for quality control that are typical in eddy-covariance processing (e.g., despiking, drop-outs, skewness and kurtosis, etc., Vickers and Mahrt 1997). Time lags due to sensor separation were compensated by maximizing covariance of scalars, and linear detrending was applied to the high-frequency data prior to flux computation (Moncrieff et al. 2005). After this initial processing (but prior to detrending), raw data for each 30-min period were saved for use in the CH₄ flux-partitioning scheme (see Sect. 2.3). Thirtyminute fluxes were also corrected for frequency losses in the measurement system (Moncrieff et al. 1997) and for density fluctuations (Webb et al. 1980). We note that the frequency loss correction adds a substantial amount to the observed fluxes in this work due to our relatively low measurement height, as shown by an average spectral correction factor of ≈ 1.2 for the fluxes of all three gas species, H₂O, CO₂, and CH₄.

Thirty-minute flux estimates were filtered for quality control prior to further analysis. Periods with wind direction between 265° and 95° were removed from the dataset, as these directions do not include the target fields in the flux footprint. The footprint model of Kormann and Meixner (2001) was used to remove 30-min periods in which the upwind distance containing 90% of the flux contribution area was greater than 350-m away from the tower, as this distance is beyond the field boundaries. Steady-state and integral turbulence characteristics tests were performed to remove periods with non-stationary scalar fluxes or poorly



developed turbulence (Foken and Wichura 1996). Based on the guidelines of Mauder and Foken (2015), 30-min periods with flag values greater than 2 (on a 1–9 scale) for CH₄ flux stationarity, reference scalar (e.g., H_2O or CO_2 , see Sect. 2.3) flux stationarity, or the vertical velocity integral turbulence characteristic were removed before performing further analysis. Following previous studies that have used scalar similarity as the basis for CH₄ flux partitioning (Iwata et al. 2018; Taoka et al. 2020; Zorzetto et al. 2021), the universal flux–variance relationships were used to remove periods in which the reference scalar was affected by non-local processes (De Bruin et al. 1993). To aid our subsequent analyses of CH₄ fluxes, CO_2 fluxes were partitioned into gross primary productivity (*GPP*) and ecosystem respiration (R_{eco}) using the night-time method (Reichstein et al. 2005). This algorithm fits a relationship between night-time CO_2 fluxes (only containing R_{eco}) and temperature that is then used to separate R_{eco} from the net CO_2 flux based on the measured temperature.

Several microclimate measurements were collected on or near the eddy-covariance towers during the study period including: water-table depth, soil temperature at 2 cm depth, four-component net radiation, air temperature, relative humidity, and atmospheric pressure. However, data availability for soil temperature at the north field and four-component net radiation at the south field was poor due to instrument malfunctions (north field soil temperature available between April and early June, south field four-component net radiation available between mid-July and harvest). Additional details on these sensors can be found in Runkle et al. (2019). Daily canopy height (z_c) and leaf area index (LAI) were estimated from manually collected observations during the 2017 growing season and a growing-degree-day (GDD) model previously developed for these fields (see Reavis et al. 2021, for more information). By pairing this LAI-GDD model with the fields' PhenoCam imagery (Milliman et al. 2019), we separated the growing season into approximate crop growth stages: vegetative through early reproductive (GDD < 965 °C-day; planting to 20 June), panicle formation through heading (965 °C-day < GDD < 1370 °C-day; 20 June to 18 July), and grain filling and ripening (GDD > 1370 °C-day; 18 July to harvest), with GDD = 0 occurring on the date of planting. These separations will be used to assess changes in the relative importance of ebullition associated with phenology.

2.3 Methane-Flux Partitioning

2.3.1 Theoretical Overview

Net fluxes of CH₄ were partitioned into diffusive (i.e., plant-mediated transport and diffusion from the water column) and ebullitive subcomponents using the method and program code of Iwata et al. (2018) (see Fig. 1 for a conceptual overview). This method is based on the concept of local scalar similarity, which is generally satisfied for homogeneous, flat terrain according to Monin–Obukhov similarity theory (Katul et al. 1995). The site used in this study meets these conditions, indicating that the sources and sinks of sensible heat, water vapour, and carbon dioxide are uniformly distributed within the flux footprint. After being emitted to the atmosphere these scalars are transported by the same eddies past a stationary observation point, leading to similar turbulent fluctuations between scalars. While the sources of diffusive CH₄ fluxes in rice fields are uniformly distributed (Fig. 1a, teal arrows), this situation is likely not the case for ebullitive CH₄ fluxes, as ebullition is generally heterogeneous in both space and time (Fig. 1a, bubbles and red arrow) (Christensen et al. 2003; Baird et al. 2004; Comas and Wright 2012). The presence of ebullition thus violates local scalar similarity, resulting in dissimilar fluctuations of CH₄ when compared to the other scalars associated with an eddy.



We note that this conceptual framework does not suggest that ebullition events are spatially coordinated, but rather that ebullition events that occur in various areas of the footprint are periodically sampled by the eddy-covariance system. Critically, the fetch of the eddy-covariance system must be spatially homogeneous during the measurement period in order to attribute these abrupt changes in CH₄ source strength to ebullition events instead of changes in footprint composition.

Raw high frequency data (Fig. 1b-d) can be decomposed into eddy scales using the orthonormal wavelet transform. Briefly, wavelet analysis extracts frequency information from a time series while maintaining information on where fluctuations of a given frequency occur in time (Foufoula-Georgiou and Kumar 1994). Thus the method is ideal for examining intermittent processes (e.g., ebullition) and multiple time series, particularly when compared to the commonly used Fourier transform, which provides high-resolution frequency information but at the expense of all information in the time domain. Critically, the orthonormal wavelet transform also preserves statistical properties of the original time series such as variance and covariance without generating redundant information, enabling flux computation directly from the resulting wavelet coefficients (Scanlon and Albertson 2001). The magnitude of coefficients is indicative of the fluctuation occurring at a given frequency at a specific point in time, and thus CH₄ wavelet coefficients can be compared to wavelet coefficients of another scalar at the same time scale and time location to assess scalar similarity and identify eddies associated with ebullition (Fig. 1e, f). In the remainder of this section we describe the most salient details of the method of Iwata et al. (2018), followed by modifications we made to the original method in Sect. 2.4. The reader is referred to the original text for more information, including the program code used for partitioning, which is freely available at http:// science.shinshu-u.ac.jp/~hiwata/program.html (v2.0 was used in this work; while v3.0 is now available, its changes are mostly relevant for analyzing closed-path CH₄ measurements).

2.3.2 Partitioning Method

The 20 Hz time series are first truncated in order to satisfy the logarithmic uniform spacing for discretizing wavelet scales (see more explanation below), leaving the first \approx 27.3 min of each 30-min period available for analysis. Missing values in the raw time series were filled by linear interpolation with random noise. Point-by-point conversion (Detto and Katul 2007) was applied to sonic temperature and gas density data to account for variations in air density (i.e., as analogous to the density corrections of Webb et al. (1980) but applied to high-frequency data), and an additional spectroscopic correction was applied to the CH₄ data (Detto et al. 2011; McDermitt et al. 2011). Wavelet coefficients were then calculated using the orthonormal wavelet transform.

$$W_x^{j,i} = \int_{-\infty}^{\infty} x(t)\psi_{j,i}(t)dt \tag{1}$$

where x(t) is the time series of the scalar of interest (e.g., vertical velocity component, sonic temperature, H₂O, CO₂, or CH₄), $\psi_{j,i}$ is the wavelet function, j is the scale parameter, i is the time location, and W_x is the wavelet coefficient for scalar x at scale j and time location i. The wavelet function, $\psi_{j,i}$, is given by a mother wavelet function that is dilated (i.e., stretched) according to j and translated across all time locations i,

$$\psi_{j,i}(t) = \frac{1}{\sqrt{2^j}} * \psi\left(\frac{t - 2^j * i}{2^j}\right) \tag{2}$$



where ψ is the mother wavelet. The method of Iwata et al. (2018) utilizes the Haar mother wavelet, which is the simplest wavelet form and is useful for its differencing characteristics and localization in time (Foufoula-Georgiou and Kumar 1994; Scanlon and Albertson 2001). Thus, the scale parameter j controls the frequency that is detected by the transform while the time location i controls where in the time series the wavelet function is centred. In practice, the orthonormal wavelet transform is implemented by discretizing j into integer values j=1,2,...,J (where the total number of measurements in the time series is 2^J) and using a pyramidal algorithm to recursively filter the signal into high pass (i.e., wavelet coefficients) and low pass (the coarse-grained signal resulting from block-averaging) components (Mallat 1989). The result is 2^{J-j} wavelet coefficients at each scale j for a total of 2^J-1 coefficients. Wavelet coefficients can be interpreted as the fluctuations in the original signal over a time scale that becomes progressively longer as the transform proceeds.

After applying the wavelet transform to each scalar of interest, local scalar similarity is assessed by comparing CH₄ wavelet coefficients with those of a reference scalar (e.g., H₂O, CO₂, and/or sonic temperature) at the same scale and time location. Of the three reference scalars initially examined in the development of the partitioning method, Iwata et al. (2018) recommended that H₂O be used because (1) scalar similarity between CH₄ and sonic temperature was influenced more often by non-local processes, and (2) CO₂ fluxes at their lake site were not of a sufficient magnitude for CH₄ and CO₂ to have strong scalar similarity even in the absence of ebullition. To characterize the relationship between CH₄ and the reference scalar in each 30-min period, coefficients within a selected spectral range are used to fit an iteratively reweighted linear regression model. This spectral range is defined in terms of a normalized frequency

$$f_n = \frac{z_m}{t_c u} \tag{3}$$

where z_m is the measurement height (m), u is the mean wind speed (m s⁻¹), t_s is the time scale of the coefficient (s; the length of time the coefficient spans), and f_n is the normalized frequency (dimensionless). The lower and upper boundaries of this normalized frequency range $(f_{n,LB})$ and $f_{n,UB}$, respectively) were determined by initial spectral analysis to be 0.003 and 1, as CH₄ wavelet coefficients between these frequencies were responsible for transporting a majority of the CH₄ flux and generally had strong coherence with reference scalar wavelet coefficients (see Online Resource 1a, c, e). CH₄ coefficients at all frequencies greater than $f_{n,LB}$ are then used to partition the CH₄ flux into diffusive and ebullitive components based on their distance from the iteratively reweighted linear regression line of best fit. The threshold for how far a coefficient must fall from the line of best fit to be considered 'dissimilar' enough to derive from ebullition is given in terms of the root-mean-squared deviation about the line of best fit during periods in which ebullition is not apparent (RMSD; see Sect. 2.3.3 for details on empirical determination of this parameter). Coefficients that fall farther than ± 3 RMSD from the line of best fit are considered ebullitive, while all other coefficients are attributed to diffusive processes (see Fig. 1e, f). While Iwata et al. (2018) found that the partitioning results were sensitive to the multiplier defining the threshold, three standard deviations from the mean response (i.e., the line of best fit) should contain 99.7% of the variance associated with non-ebullitive coefficients, assuming that they are normally distributed. Therefore, we deem a multiplier of 3 as sufficient for determining the ebullition threshold in terms of the empirical RMSD.

Once the ebullitive CH_4 wavelet coefficients have been identified (i.e., the points falling outside the red dashed lines in Fig. 1e, f), the ebullitive flux (F_{eb}) is calculated by summing the product of the vertical velocity component and CH_4 wavelet coefficients across all time



locations at each scale and then summing this scale-wise covariance over all scales of the transformation

$$F_{eb} = \frac{1}{N} \sum_{i} \sum_{i} W_{w}^{j,i} W_{m}^{j,i} \delta^{j,i}$$
 (4)

where W_w and W_m are the vertical velocity component and CH₄ coefficients, respectively, N is the total number of coefficients in the period, and δ is an indicator function for whether the coefficient at location j,i is considered ebullitive, taking on a value of 1 when the coefficient falls beyond the ebullition threshold and zero otherwise. The diffusive flux (F_{diff}) is calculated as the difference between the total flux and F_{eb} . In a final step, the method of Finkelstein and Sims (2001) is used to estimate random error in both the diffusive and ebullitive flux estimates.

2.3.3 Determination of Empirical Ebullition Threshold

As discussed in Sect. 2.3.2, determining the ebullition threshold for CH₄ wavelet coefficients requires an empirical parameter, RMSD, which represents the average deviation from the line of best fit between the wavelet coefficients for CH₄ and the reference scalar during 30min periods in which ebullition is minimal. We selected these 'non-ebullitive' periods by visually screening the 20-Hz gas concentration data to ensure global similarity between CH₄ and the reference scalars, which we assume holds when ebullition is not significant (Taoka et al. 2020). Gas concentration data were inspected in both the time domain (Fig. 2) and wavelet domain (Fig. 3) for global similarity. Each time series was required to lack sporadic fluctuations unique to CH₄, as their presence indicates that ebullition is potentially occurring (Fig. 2a, d, as contrasted with Figs. 2b, c and e, f respectively). Scatterplots of W_m and wavelet coefficients of each reference scalar (W_a for H_2O , W_c for CO_2 , W_x when referring to the reference scalars generally) with data points coloured by f_n were then examined for the same period; if coefficients generally fell in a cluster around the line of best fit and no high frequency coefficients were far outside the main body of this cluster (Fig. 3e, f and g, h), the period was deemed suitable for RMSD fitting. See Figs. 2 and 3 for a comparison of periods containing apparent ebullition with non-ebullitive periods used for RMSD fitting. While not explored in this work, we note that the process of non-ebullitive period selection could be streamlined by screening all CH₄ concentration time series using a median absolute deviation test (MAD, e.g., Papale et al. 2006; Schaller et al. 2017). Such a rule-based approach should lead to a more objective and automated screening process in which periods with sporadic fluctuations in CH₄ concentration are automatically removed from consideration for RMSD fitting.

The two previous studies using this partitioning method have calculated unique *RMSD* values for approximately each month of the study by averaging the *RMSD* of non-ebullitive periods falling within that sub-period (see Table 1). The findings of Hwang et al. (2020) indicate that accounting for temporal variation in the *RMSD* is critical, as their values increased by ninefold over the course of the growing season (reported values for *RMSD* based on H₂O ranged from 2 to 11 times the empirical *RMSD* reported by Iwata et al. (2018), see Table 1). Following Taoka et al. (2020), we initially calculated a unique empirical *RMSD* for each month of each site's dataset to account for any temporal or site-specific variation in the degree of similarity between CH₄ and the reference scalars. We selected 3–10 such 30-min periods for each month, depending on the results of the aforementioned screening process. The *RMSD* values resulting from the iteratively reweighted least-squares linear



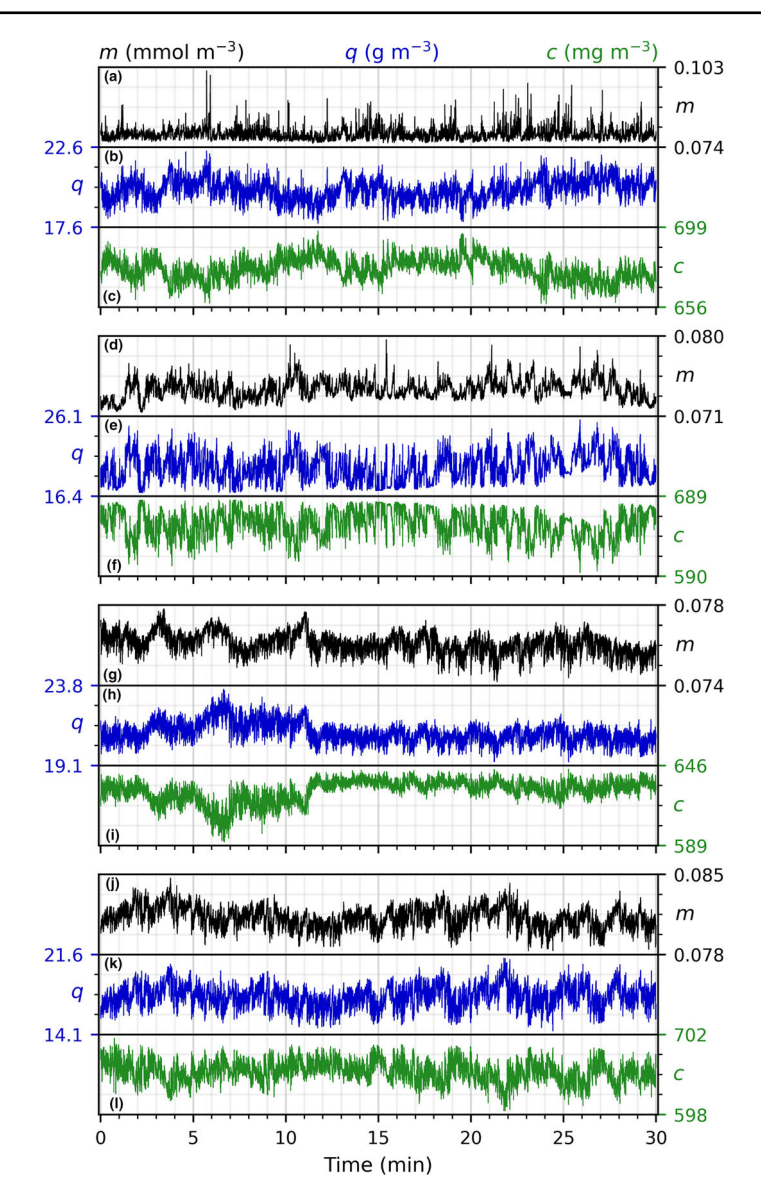
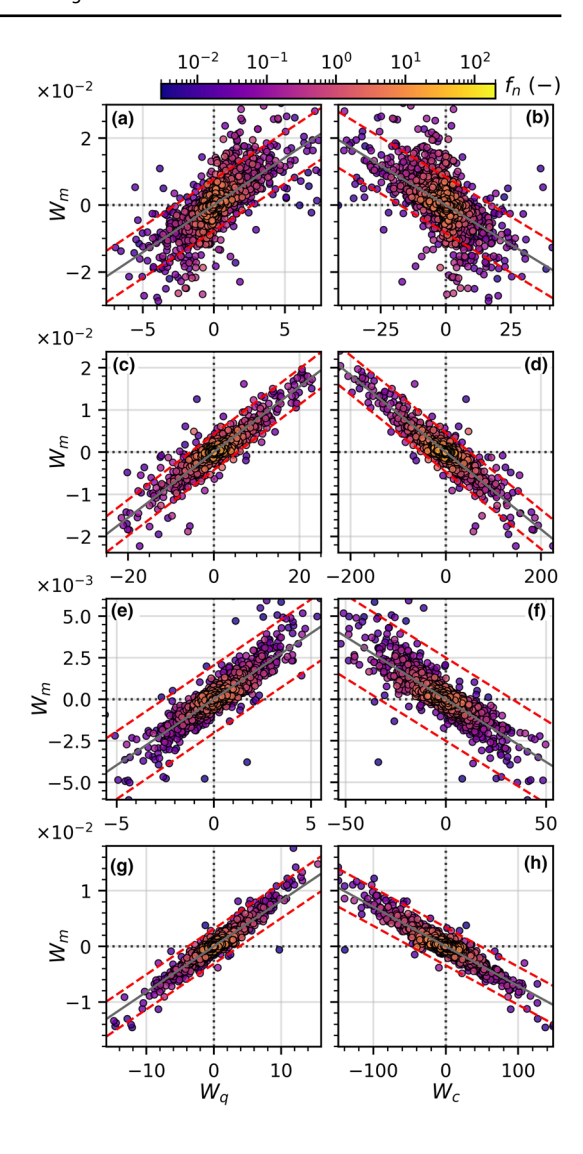


Fig. 2 Examples of periods with apparent ebullition (6 August 1600 LT, Monin–Obukhov stability parameter $(\zeta) = -0.012$, friction velocity $(u_*) = 0.51$ m s⁻¹, **a**-**c**; 1 July 1530 LT, $\zeta = -0.076$, $u_* = 0.16$ m s⁻¹, **d**-**f**) and without apparent ebullition (30 June 1630 LT, $\zeta = 0.006$, $u_* = 0.55$ m s⁻¹, **g**-**i**; 28 June 1000 LT, $\zeta = -0.001$, $u_* = 0.30$ m s⁻¹, **j**-**l**) in the time domain, given traces of methane (m), water vapour (q), and carbon dioxide (c). Note that 6 August 1600 LT is a period relatively dominated by ebullition for this site, whereas 1 July 1530 LT is a more typical period in which some ebullition is occurring (intermittent sporadic fluctuations in **d**) but diffusive processes contribute substantially to the total flux



Fig. 3 Wavelet coefficient scatterplots for example periods shown in Fig. 2. Periods with apparent ebullition: 6 August 1600 LT, $\bf a$ and $\bf b$; 1 July 1530 LT, $\bf c$ and $\bf d$. Periods without apparent ebullition: 30 June 1630 LT, $\bf e$ and $\bf f$; 28 June 1000 LT, $\bf g$ and $\bf h$. In each row, methane wavelet coefficients (W_m) are compared with those of water vapour (W_q) left column) and carbon dioxide (W_C) , right column) to assess scalar similarity



regressions between wavelet coefficients of CH₄ and the reference scalars in each of these 30-min periods were then averaged within each month (see Table 1). While not enough studies have been conducted to characterize an expected range of values for *RMSD*, our values based on H₂O (north field: 0.00107–0.00274, south field: 0.000729–0.00272) do fall near the program default *RMSD* (0.000803) and within the range reported by Hwang et al. (2020, 0.00145–0.00927). These month-specific mean *RMSD* values were then used to calculate the ebullition threshold and subsequently to partition the CH₄ flux. However, upon more detailed inspection of the program code and the results from the partitioning method (implemented as described in this section), we found that several modifications were necessary to adapt the method to our site and improve the accuracy of ebullition estimates.



Table 1 Parameter values reported by previous studies* and calculated for this study following the original partitioning program methodology

| Study | Sub-period mean non-ebullitive RMSD | $f_{n,LB}$ | |
|-----------------------|---|------------|--|
| Iwata et al. (2018) | Two-week period in August: $0.000803(q)$ | 0.003 | |
| | Two-week period in August: 0.000859 (T _{sonic}) | | |
| Hwang et al. (2020)** | Before rice transplanting: 0.001454 0.007 | | |
| | Before mid-season drainage: 0.001522 | | |
| | During mid-season drainage: 0.007894 | | |
| | After mid-season drainage: 0.009625 | | |
| This study*** | June: 0.00107 (q), 0.00119 (c) 0.003–0.030 | | |
| | July: 0.00274 (q), 0.00270 (c) | | |
| | August: 0.00121 (q), 0.00145 (c) | | |

^{*}Taoka et al. (2020) also used this partitioning method, but parameter values were not reported. T_{sonic} : sonic temperature

2.4 Modifications to the Partitioning Method

2.4.1 Formulation of Normalized Frequency

The original formulation for the normalized frequency, f_n , includes no information on surface roughness, as the vertical dimension defining turbulent transport in Eq. (3) is z_m . When considering a lake, any emergent vegetation that is present tends not to protrude far above the surface, and surface roughness (i.e., aerodynamic roughness length when no canopy is present; 0.002-0.006 m for open water, Monteith and Unsworth 2013, Table 16.1) is negligible when compared to z_m . In the case of observations made over an actively growing canopy, the mean wind speed will approach zero at some height above the ground surface due to increased surface roughness. The most relevant vertical dimension for defining turbulent transport in this case is $z_m - z_d$, where z_d is the zero-plane displacement (Monson and Baldocchi 2014; approximated as $2z_c/3$ for rice, Gao et al. 2003). This term is especially critical to account for in our observations, as our z_m is substantially closer to the ground than that used in Hwang et al. (2020) (≈ 2.3 m versus 10 m). We therefore modified Eq. 3 to account for these changes in the relative location of the sonic anemometer within the vertical wind profile over the course of crop development,

$$f_n = \frac{z_m - z_d}{t_s u} \tag{5}$$

We also note that in the program code, a 10-Hz measurement frequency (i.e., interval between data points is 0.1 s) is hard coded into the calculation of t_s in several places; we modified this program variable to 0.05 s because our data were collected at 20 Hz. These changes had the net effect of shifting the covariance and coherence spectra toward lower frequencies, meaning that more wavelet coefficients of longer time scales are generally excluded by the frequency bounds when calculating f_n using Eq. 5 as compared to using Eq. 3 (see Online Resource 1b, d, f).



^{**} All *RMSD* values reported by Hwang et al. (2020) based on q as reference scalar

^{****}RMSD values reported here are for the north field, using Eq. 3 to calculate f_n , and the range of $f_{n,LB}$ reported here pertain to the modified method (i.e., using Eq. 5)

2.4.2 Selection of Reference Scalars

While examining raw time series plots and wavelet coefficient scatterplots to find non-ebullitive periods for RMSD fitting, we found that the suitability of using each of the reference scalars in the partitioning method was dependent on the magnitude of the associated net flux of that reference scalar in each 30-min period. Similar to the findings of Iwata et al. (2018) with respect to CO_2 fluxes, scalar similarity between CH_4 and H_2O , CO_2 , or sonic temperature broke down even in the absence of ebullition when the magnitude of the reference scalar flux was small. We emphasize that the magnitude, not direction, of the flux dictates this effect for CO_2 and sonic temperature: a net downward flux of CO_2 or H only changes the slope of the W_m - W_x relationship from positive to negative. In the wavelet coefficient scatterplots this breakdown in scalar similarity is marked by little to no linear relationship between W_m and W_x (Fig. 4a) or large scatter about the line of best fit (Fig. 4b) despite the absence of sporadic fluctuations in the CH_4 time series. Without adequate scalar similarity as a baseline for comparison in these cases, the method appears to overestimate the true ebullitive flux, flagging many coefficients as ebullitive despite little evidence of sporadic ebullition in the time series of the raw data.

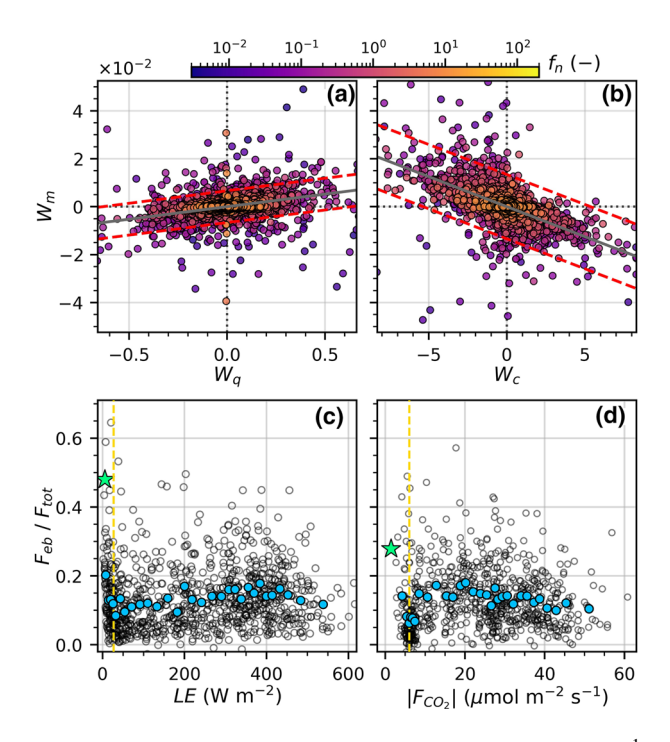


Fig. 4 Examples of periods in which CH₄-H₂O (3 July 0030 LT, $\zeta = 0.031$, $u_* = 0.23$ m s⁻¹, **a**) and CH₄-CO₂ (12 July 1900 LT, $\zeta = 0.065$, $u_* = 0.20$ m s⁻¹, **b**) scalar similarity breaks down due to low magnitude of the respective reference scalar fluxes. The relationship between fractional ebullition (i.e., ebullitive flux divided by total flux) and reference scalar flux is shown for water vapour and carbon dioxide in **c** and **d**, respectively, for the north field, and determined via the modified partitioning method. Blue circles are bin averages. Example periods shown in **a** and **b** have been plotted as green stars in **c** and **d**, respectively. The lower thresholds defining adequate scalar similarity (dashed yellow lines in **c** and **d**) were identified manually



Over different time scales, each of the H_2O , CO_2 , and sensible heat fluxes varies uniquely, which has important implications for which reference scalar is most appropriate to use for CH_4 flux partitioning in any given 30-min period. Under continuously flooded conditions, most of the incoming radiant energy is partitioned toward LE rather than H. Because low-magnitude H is the norm at our site, scalar similarity between CH_4 and sonic temperature often does not hold, and thus sonic temperature is not a suitable reference scalar at our site. By the same token H_2O is a particularly suitable reference scalar during the day and early evening hours, as LE tends to be large during these times. However, LE typically decreases as the night progresses, weakening the scalar similarity between H_2O and CH_4 and making H_2O less suitable as a reference scalar at night.

Net CO₂ flux measurements include both photosynthesis (CO₂ uptake, i.e., GPP) and respiration (CO₂ release, i.e., R_{eco}) and show large variation in both sign and magnitude across the diel cycle. The magnitude of CO₂ fluxes due to each of these individual processes in an actively growing crop should generally be larger than in lakes. Thus, CO₂ should be more suitable as a reference scalar when partitioning CH₄ fluxes from rice as compared to other lake or less productive wetland ecosystems. During daylight hours net CO2 exchange is dominated by GPP, resulting in large net downward CO₂ fluxes and a negative slope for the W_m - W_c relationship (because the net CH₄ flux is positive in all periods in this analysis). At night only R_{eco} occurs, resulting in net upward CO₂ fluxes and a positive slope for the W_m - W_c relationship. During each of these times of day we found that magnitudes of CO₂ fluxes were sufficiently large, such that scalar similarity between CO₂ and CH₄ was strong in the absence of ebullition. As with the case of H₂O-CH₄ similarity during night-time hours, CO₂-CH₄ similarity was not maintained in the absence of significant ebullition when net CO_2 fluxes were near zero (i.e., periods in which GPP and R_{eco} are of similar magnitude, generally around sunrise and sunset at our site). We also note that partitioning based on CO₂ is not currently an option in the published program code, so we modified it to include the use of CO₂ as a reference scalar for partitioning.

Because ebullitive fluxes should not be a function of the latent heat flux or the CO2 flux, we plotted the fractional ebullition estimates (i.e., ebullitive flux divided by total flux; F_{eb}/F_{tot}) against the fluxes of their corresponding reference scalars to determine the flux magnitudes at which scalar similarity with CH₄ breaks down (Fig. 4c, d). As the magnitudes of the latent heat flux and the CO₂ flux increases above zero, F_{eb}/F_{tot} rapidly declines. We assume that once F_{eb}/F_{tot} has declined to a level comparable with that at higher reference scalar flux values, there is enough scalar similarity with CH₄ for the reference scalar to be used to partition CH₄ fluxes. Using the data shown in Fig. 4c and d, we visually identified threshold values that approximately define the minimum reference scalar flux magnitude for adequate scalar similarity with CH₄. These values were 27 W m⁻² for latent heat fluxes and 6 µmol m⁻² s⁻¹ for CO₂ fluxes. If either of these fluxes were less than the threshold, the ebullition estimate for that reference scalar was flagged and omitted from further analysis. In post-processing, we create a 'harmonized' time series of partitioning results in which H2O is preferentially used as the reference scalar if latent heat fluxes are of sufficient magnitude; CO₂ is used as the reference scalar in cases where LE is not of sufficient magnitude but the CO2 flux is.

2.4.3 Development of a Dynamic Ebullition Threshold

As we analyzed the partitioning results based on these month-specific ebullition thresholds, several observations led us to hypothesize that the threshold should be more dynamic to accurately detect ebullition. When plotting the month-specific ebullition thresholds on the wavelet



coefficient scatterplots for each period, we found that the ebullition threshold often either (a) failed to contain the spread of non-ebullitive coefficients in a period, subsequently classifying many non-ebullitive coefficients as ebullitive during periods when minimal ebullition was evident in the raw time series, or (b) fell so far beyond the spread of non-ebullitive coefficients that even the higher frequency coefficients associated with sporadic fluctuations in CH₄ fell within the threshold and were not considered as ebullitive. Therefore, we calculated RMSD based on each reference scalar in each 30-min period (RMSD_x) to examine how this parameter varied over shorter time scales as compared to a threshold that captures variation only over a monthly time scale. When examining wavelet coefficient scatterplots spanning a range of $RMSD_x$, we found no consistent relationship between the magnitude of $RMSD_x$ and the presence of apparent ebullition. While the magnitude of $RMSD_x$ should increase as a result of ebullition, it is calculated from wavelet coefficients whose range of magnitude is largely dependent on the global variance of the 30-min time series (see Online Resource 2), as the wavelet transformation decomposes this global variance across finer time scales of fluctuation. The diel pattern in CH₄ standard deviation (Online Resource 7e) corroborated this relationship, showing similar behaviour to that of $RMSD_q$ and $RMSD_c$. Thus $RMSD_x$ in any period carries information on the global variance of CH₄, and the ebullition threshold should account for changes in wavelet coefficient magnitude that are due to changes in 30-min variance rather than ebullition. While the MAD has also been used as a metric for detecting sporadic events in time series (Papale et al. 2006), we found that 30-min MAD values were much smaller in magnitude than their corresponding $RMSD_x$ values (necessitating a multiplier much larger than 3 to fit a reasonable ebullition threshold) and did not distinguish well between ebullitive and non-ebullitive periods. Therefore, we chose to continue with the use of $RMSD_x$ for CH_4 flux partitioning.

We further explored the relationship between $RMSD_x$ and the standard deviation of CH₄ (σ_m) to develop a dynamic ebullition threshold as a function of σ_m (see Fig. 5). When considering all best quality 30-min periods, we found strong linear relationships between $RMSD_q$ and σ_m ($R^2 = 0.60$, p < 0.01; grey dashed line in Fig. 5a) as well as between $RMSD_c$ and σ_m ($R^2 = 0.75$, p < 0.01; grey dashed line in Fig. 5b). While the mean responses of these relationships across all 30-min periods (i.e., the linear regression slopes) are influenced by periods with significant ebullition, this finding suggests that a linear model is suitable for describing the relationship. We then fit these same $RMSD_x - \sigma_m$ linear regression relationships on only using the periods we had previously identified as non-ebullitive (pink dashed lines in Fig. 5). The slope of these relationships defines the typical deviation expected around the line of best fit when ebullition is not significant, accounting for the change in spread of wavelet coefficients due to global variance of CH₄. Critically, it should be noted that using the observed σ_m to fit the ebullition threshold in each 30-min period may underestimate the ebullitive flux because the presence of significant ebullition would increase σ_m and thus the width of the ebullition threshold. However, for simplicity we do not attempt to resolve this issue here (see Sect. 4.1 for more discussion). Additionally, it is somewhat subjective to visually identify non-ebullitive periods, and these periods make up a relatively small sample size (n = 21 for the north field, n = 11 for the south field) when compared to the total number of best quality 30-min periods.

We therefore decided to characterize the $RMSD_x$ – σ_m relationships using quantile regression on all best quality 30-min periods as an alternate means of developing a dynamic ebullition threshold. Briefly, quantile regression provides regression slopes between a set of response and predictor variables across different parts of the response variable distribution (Cade and Noon 2003). For example, the 5th percentile quantile regression slope describes the response of the lowest 5% of response variable observations ($RMSD_x$) to the predictor



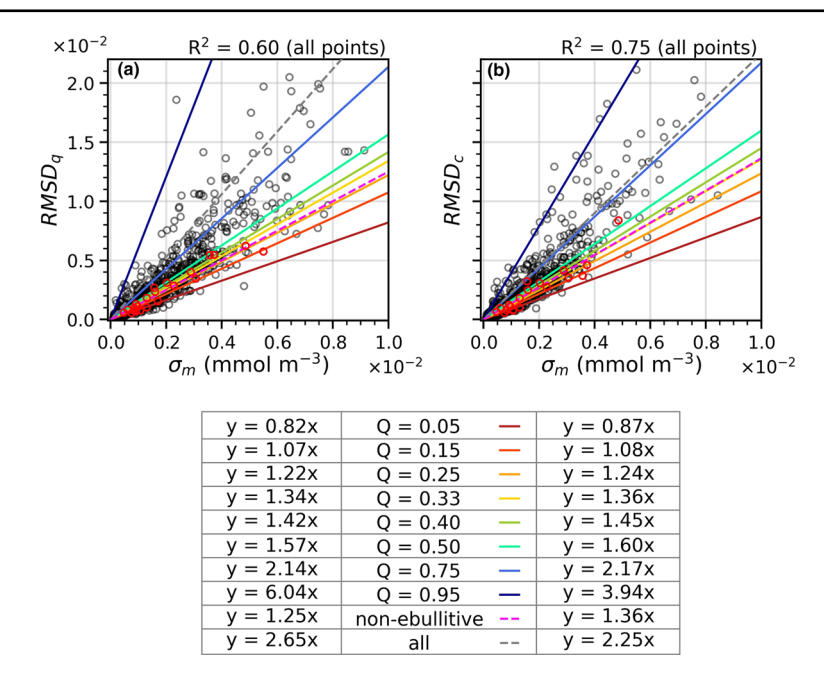


Fig. 5 $RMSD_x - \sigma_m$ relationships for **a** water vapour and **b** carbon dioxide as reference scalars. Open black circles are 30-min periods from the north field meeting all quality requirements. Solid lines show quantile regression slopes ranging from the 5th (i.e., Q = 0.05) to 95th (i.e., Q = 0.95) percentile. Manually identified non-ebullitive periods (see Sect. 2.3.3) are shown in red circles, and the pink dashed line is the corresponding linear regression line of best fit for these periods. The grey dashed line is the linear regression line of best fit for all periods displayed

variable (σ_m), with the number of observations included in the regression increasing as the quantile of interest increases. Thus the quantile regression slopes for the lower portion of the $RMSD_x$ distributions are an alternate, objective means of generating a dynamic ebullition threshold, assuming that ebullition is the main factor driving increased $RMSD_x$ at any given value of σ_m .

To determine which quantile response would be most appropriate for defining the dynamic ebullition threshold, we fit the $RMSD_x-\sigma_m$ quantile regression model using a range of quantiles (solid lines in Fig. 5) and compared these slopes to the $RMSD_x-\sigma_m$ linear regression slope from the visually identified non-ebullitive periods. For both $RMSD_q-\sigma_m$ and $RMSD_c-\sigma_m$ at the north field, the linear regression slope from non-ebullitive periods fell near the 33rd percentile slopes from quantile regression (slopes closer to 40th and 50th percentile slopes for the south field). However, several of the visually identified non-ebullitive periods had $RMSD_x$ as large as the value predicted by the 50th percentile slope or value as low as that predicted by the 15th percentile slope (red circles in Fig. 5). Based on these findings, we used the non-ebullitive $RMSD_x-\sigma_m$ linear regression slopes as a baseline for the new dynamic ebullition threshold and tested a range of thresholds (15th–50th percentile slopes for the north field, 25th–75th slopes for the south field) in the sensitivity analysis of the method (see Sect. 2.5).

Hereafter, the partitioning method as described in Sect. 2.3.2 is referred to as the 'original' method, although we did use both H_2O and CO_2 as reference scalars in the original method to increase the number of best quality observations. The partitioning method with all modifications described in this section will be referred to as the 'modified' method.



2.5 Method Uncertainties and Sensitivity Analysis

Whether in the original form developed by Iwata et al. (2018) or with the modifications we proposed in Sect. 2.4, the empirical nature of this CH₄ flux partitioning method leaves room for substantial uncertainty in the resulting ebullitive flux estimates. As discussed above, the width of the ebullition threshold is the $RMSD_x$ parameter multiplied by some integer (3 in the original presentation of the method). This width, representing how dissimilar W_m must be from W_x in order to be considered ebullitive, is somewhat arbitrary, and no studies have rigorously examined the sensitivity of the resultant ebullitive flux estimates to changes in ebullition threshold width. Furthermore, the method has only been applied a handful of times and has not yet been validated against independent observations of ebullition. Collectively these points illustrate that the parameters of the partitioning method have not been fully explored and are largely unconstrained. In the absence of further ground-based validation of the method, we conducted a sensitivity analysis by running the modified partitioning method using a range of values for the primary parameters, $f_{n,l,B}$ and $RMSD_x$, to characterize the magnitude of possible uncertainty associated with the ebullitive flux estimates. While $f_{n,UB}$ could also potentially be modified, we focused on $f_{n,LB}$ because of its relevance to the duration of ebullition events (see below). In the following subsections we describe how modifying $f_{n,LB}$ and $RMSD_x$ can potentially impact the partitioning results and how we selected a range for each parameter to use in the sensitivity analysis.

2.5.1 Lower Frequency Bound

It is critical to recall that the lower frequency bound, $f_{n,LB}$, determines which wavelet coefficients are a) used to fit the iteratively reweighted linear regression and b) included in the partitioning estimate (see Sect. 2.3.2). In light of the former, modifying this parameter changes the value of RMSD in each period because a different set of W_m-W_x regression model residuals is used for the calculation. Thus, regardless of which method is used to calculate $RMSD_x$ for the ebullition threshold, changes in $f_{n,l,B}$ also indirectly impact the width of the ebullition threshold. We therefore first investigated changes in $RMSD_x$ as a function of $f_{n,LB}$. While RMSD_x did tend to decrease slightly as $f_{n,LB}$ increased (see Online Resource 3), these indirect changes in ebullition threshold width due to $f_{n,LB}$ will be encompassed by the sensitivity analysis on $RMSD_x$ (see below), so we do not attempt to characterize uncertainty in the method due to this specific interaction. The more salient impact of $f_{n,LB}$ on partitioning estimates is selecting which wavelet coefficients should be included in the partitioning. In our initial attempt to select an appropriate value for $f_{n,LB}$ (Sect. 2.3.2, Online Resource 1), we followed the method of Iwata et al. (2018), in which $f_{n,LB}$ is determined by examining CH₄ flux cospectra and CH₄-reference scalar coherence spectra so as to include most of the flux transporting region without including frequency regions that generally lack adequate scalar similarity. While these criteria are important, the wavelet coefficients represent fluctuations over discrete periods of time, which is especially critical to consider when identifying a process with large spatiotemporal variation such as ebullition. It is therefore also important to constrain $f_{n,LB}$ in the context of the expected time scale for ebullition events.

When examining the W_m – W_x wavelet coefficient relationships and time series for 30-min periods across the growing season, we often noticed that the lowest frequency coefficients were classified as ebullitive despite no clear indication of ebullition events occurring over such long time scales (> 2 min) in the 20-Hz time series. By comparing the f_n values at each time scale of the wavelet transformation for all best quality periods to potential values for $f_{n,LB}$, one can assess how frequently coefficients from each time scale are included in



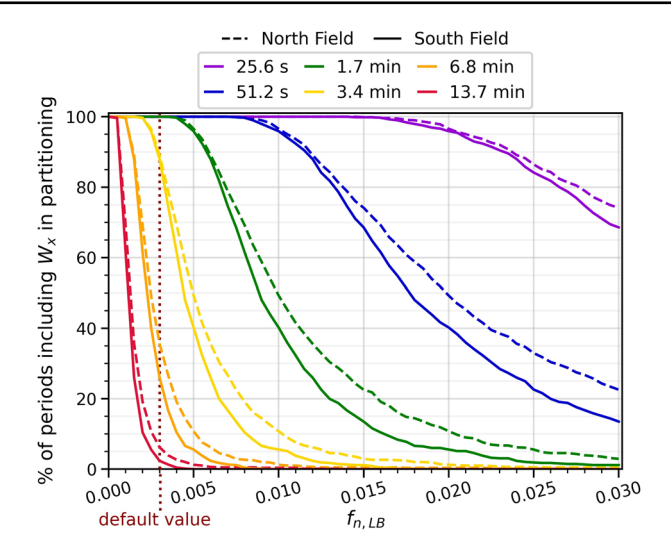


Fig. 6 Percentage of best quality 30-min periods including wavelet coefficients from a selection of time scales as a function of lower frequency bound, $f_{n,LB}$

the partitioning. As shown in Fig. 6, at $f_{n,LB} = 0.003$ (the program default value), 90% of periods include wavelet coefficients spanning \approx 3.4 min, while 36% and 3% of best quality periods include coefficients spanning \approx 6.8 and \approx 13.7 min, respectively. Because we found little to no clear visual evidence of ebullition events spanning such long durations in the raw CH₄ concentration time series, we propose that it is also critical to interpret $f_{n,LB}$ as the longest time scale over which a sporadic ebullition event could occur and be detected by an eddy-covariance system.

Unfortunately, few datasets have reported on the duration of sporadic ebullition events to further constrain our values for $f_{n,LB}$. Iwata et al. (2018) suggested that the time scale of ebullition is typically less than a few minute, and recent static chamber measurements of CH₄ fluxes in rice showed ebullition events predominantly lasting between 10 and 40 s with a few large events lasting approximately 1 min (Kajiura and Tokida 2021). The 1 Hz gas concentration measurements from that study did not show monotonic change with time during these longer duration ebullition events, suggesting the presence of multiple discrete bubbling events in succession that are identifiable as distinct peaks within these larger events. Guided by this information and Fig. 6 we ran the partitioning method using a range of values for $f_{n,LB}$ spanning 0.003 to 0.030. We set 0.030 as the maximum value tested to exclude wavelet coefficients spanning ≈51 s or longer in most periods, which is consistent with previous observations that scalar similarity diminishes at event durations greater than 60 s (Ruppert et al. 2006). In most cases, increasing $f_{n,LB}$ would tend to decrease the fractional ebullition in any given period because more W_m coefficients would be excluded from the partitioning. However, plotting cospectra for the ebullitive CH₄ fluxes revealed that the longer time scale (i.e., lower frequency) ebullitive fluxes in some 30-min periods were negative, which is unclear to interpret. Thus when these coefficients were filtered from the partitioning, the calculated fractional ebullition increased. This effect further underscores the need to examine the sensitivity of the method to $f_{n,LB}$ and to constrain the duration of sporadic ebullition events in the context of the spatiotemporal resolution of an eddy-covariance system.



2.5.2 Ebullition Threshold Width

During initial development, Iwata et al. (2018) performed a sensitivity test by running the partitioning method with ebullition threshold multiplier values of 2 and 4 in place of the original value, 3. These modifications changed the magnitude of the diffusive flux by 10%, indicating a need to further investigate and constrain sensitivity related to ebullition threshold width. While modifying either the multiplier or $RMSD_x$ would have the effect of changing ebullition threshold width, we focus on $RMSD_x$ because our method modifications have introduced a framework in which it is readily modified. Furthermore, modifying RMSD_r is still comparable with modifying the multiplier, as taking the ratio of any value for $RMSD_x$ to the baseline value and multiplying it by 3 yields an equivalent ebullition-threshold multiplier (i.e., the multiplier if all changes in ebullition threshold width were attributed to the multiplier rather than $RMSD_x$). Visualizing the partitioning method graphically (see Fig. 1e and f), we would expect fractional ebullition and $RMSD_x$ to have an inverse relationship: when increasing (decreasing) $RMSD_x$ in a given period, the ebullition threshold will be wider (narrower), thus containing (excluding) more wavelet coefficients and decreasing (increasing) the proportion of the total flux that is classified as 'ebullitive'. However, similar to the point raised at the end of the previous paragraph, the net flux due to W_m and W_w at a given scale and time location (see Eq. 4) could be negative. If such points were counted as diffusive (ebullitive) due to increased (decreased) $RMSD_x$, the resultant fractional ebullition would increase (decrease). These two small examples show that the effects of modifying $RMSD_x$ on partitioning results may not always be straightforward and require further investigation.

As discussed in Sect. 2.4.3, our modified method uses the slope of the $RMSD_x - \sigma_m$ relationship from a selection of periods to generate a value for $RMSD_x$ in each 30-min period. To facilitate direct comparison with the original partitioning method, we used the manually identified non-ebullitive periods to fit this relationship, as those periods are common to both methods of fitting $RMSD_x$ (see Sects. 2.3.3 and 2.4.3). With this ebullition threshold width as a baseline in our modified method, we examined sensitivity to $RMSD_x$ by running the partitioning method with the quantile regression slopes falling on either side of the non-ebullitive $RMSD_x - \sigma_m$ line of best fit (see Fig. 5). We selected the minimum and maximum slopes for the sensitivity analysis by plotting the resultant ebullition thresholds on wavelet coefficient scatterplots (e.g., Fig. 1e and f) and visually examining where they typically fell in relation to the main body of wavelet coefficients along the W_m - W_x line of best fit. This exercise resulted in three equivalent multipliers (EM) for use in the sensitivity analysis: $EM \approx 2.3$ (15th percentile slope for the north field, 25th percentile slope for the south field, narrowest threshold), $EM \approx 2.7$ (25th percentile slope for the north field, 40th percentile slope for the south field, slightly less narrow than the baseline threshold), and $EM \approx 3.5$ (50th percentile slope for the north field, 75th percentile slope for the south field). All partitioning runs in the $RMSD_x$ sensitivity analysis were conducted at $f_{n,LB} = 0.020$, which seemed to be most appropriate value for these site-years after conducting the $f_{n,LB}$ sensitivity analysis (see Sect. 3.2).

2.6 Analysis of Biophysical Controls on Flux Partitioning

Lastly, we used the ancillary meteorological and flux observations to analyze the biophysical controls on CH₄ flux partitioning. This analysis consisted of two main steps, namely: (1) a broad, pair-wise correlation analysis across a range of the partitioning runs between the response variables of interest [i.e., total CH₄ fluxes (F_{tot}), ebullitive CH₄ fluxes (F_{eb}), and fractional ebullition (F_{eb}/F_{tot})] and all available predictor variables, and (2) development of



multiple linear regression models for our 'best' partitioning estimates. The initial pairwise correlation analysis helped us both identify the most relevant predictor variables for use in subsequent linear regression modelling and detect any changes in variable relevance stemming from changes in program parameters. Neither F_{tot} nor F_{eb} were normally distributed and both generally skewed to the right; thus, fluxes were log-transformed prior to both steps of this analysis. Based on step (1), we found a need to implement a few additional filtering steps prior to step (2). First, inspection of high frequency data from periods with low F_{tot} showed a general inconsistency in method output when F_{tot} was less than 0.01 μ mol m⁻² s⁻¹; therefore, we removed these periods from all further analysis. Second, the partitioning method occasionally returned negative values for F_{eb} ; as the interpretation of 'negative ebullition' is unclear, we omitted these periods from further analysis rather than forcing them to a value of zero. These steps left a total of 839 and 716 30-min periods from the 'best' partitioning runs meeting all quality requirements for the north and south fields, respectively.

After constructing a preliminary set of models using predictor variables identified in step (1), we assessed the relative importance of predictor variables using the R package Relaimpo (Grömping 2006), which averages sequential R^2 values across different orderings of the predictor variables in the model to identify the unique contribution of each variable to the model R^2 . In the case of all response variables of interest, 4–5 predictor variables emerged as the most important, and these predictor variables were used to construct a final set of regression models. Additionally, we examined diel variation in the partitioned fluxes and the most relevant predictor variables to aid our inference of the processes controlling ebullition. Tests for equality of means and medians on fractional ebullition across sets of partitioning runs were conducted using the stats sub-package within the Python package SciPy (Virtanen et al. 2020).

3 Results

3.1 Partitioning Estimates from Original and Modified Methods

As a preliminary step, we isolated all periods in which both H_2O and CO_2 were suitable as reference scalars to ensure that the partitioning estimates based on the two scalars were comparable (Online Resource 4). Regardless of method or parameters used, fractional ebullition based on CO_2 ($F_{eb,c}/F_{tot}$) generally showed good agreement with fractional ebullition based on H_2O ($F_{eb,q}/F_{tot}$) (R^2 values between 0.83 and 0.96), with slightly better agreement for the south field. Linear regression slopes between $F_{eb,q}/F_{tot}$ (y) and $F_{eb,c}/F_{tot}$ (x) ranged from 0.91 to 0.98, indicating a tendency for CO_2 to yield higher ebullition estimates than H_2O . However, differences between $F_{eb,q}/F_{tot}$ and $F_{eb,c}/F_{tot}$ also showed some variation by time of day. Most notably, $F_{eb,c}/F_{tot}$ was larger than $F_{eb,q}/F_{tot}$ more frequently around sunrise and sunset (Online Resource 4, orange and purple points), while the reverse was more common at night-time (Online Resource 4, green points). Although there are slight differences between partitioning estimates based on the two reference scalars, the general agreement between $F_{eb,q}/F_{tot}$ and $F_{eb,c}/F_{tot}$ across partitioning runs indicates that creating a harmonized time series using multiple reference scalars for the partitioning is a feasible approach.

To further ensure the quality of the harmonized partitioning results, we analyzed scalar similarity between CO₂ and H₂O in the wavelet domain to exclude the possibility that the ebullition detected by the partitioning program was erroneously derived from fluctuations in the reference scalar time series. As shown in Fig. 7, there was no relationship between



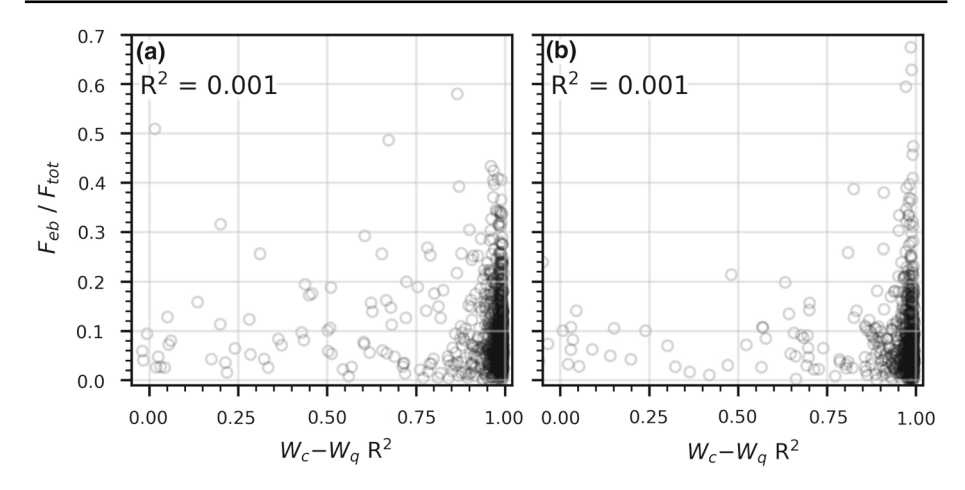


Fig. 7 The relationship between fractional ebullition (F_{eb}/F_{tot}) and the R^2 value of the iteratively reweighted linear regression between wavelet coefficients of CO_2 (W_c) and H_2O (W_q) for the north field (**a**) and south field (**b**). Data plotted are the harmonized 30-min time series for the modified method ($f_{n,LB} = 0.020$)

 F_{eb}/F_{tot} and the degree of scalar similarity between CO₂ and H₂O (as given by the W_c-W_q iteratively reweighted linear regression R^2). The vast majority of periods with poor scalar similarity between CO₂ and H₂O had previously been flagged for one reference scalar not meeting all quality requirements. For the periods in which both reference scalars met all quality requirements, the magnitude of W_c-W_q coherence (considering all W_x with $t_s < 60$ s) was consistently greater than 0.9 over the course of the day (negative during daytime, positive during night-time; data not shown). In other words, for the range of frequencies in which we would expect to observe ebullition, CO₂ and H₂O have strong scalar similarity, and are thus not likely driving the observed patterns of ebullition.

The harmonized partitioning estimates from the original and modified methods along with selected environmental variables are shown for the north and south fields in Fig. 8 and S5, respectively. Due to station outages and low F_{tot} in the early part of the season, only observations from 5 June onward are shown. At both fields, the original and modified methods generally agreed on the seasonal timing of F_{eb} and F_{eb}/F_{tot} , but the values from the original method had wider variation and larger extremes than those from the modified method for both fields across much of the study period (see Fig. 8a, b and S5a,b). As estimated from the modified method, F_{eb} remained consistently below 0.04–0.05 μ mol m⁻² s⁻¹ until the middle of heading around 9 July, whereas F_{eb} from the original method showed clear excursions above these values during the second half of June (30-min F_{eb} as high as 0.1 μ mol m⁻² s^{-1} ; see Fig. 8b), particularly at the north field. From this point in time, F_{eb} based on both methods increased to a local maximum near the beginning of grain filling (18 July), coinciding with a period of decreasing wind speed and increasing air temperature (Fig. 8c, d, S5c, d). Following this maximum, F_{eb} decreased for the remainder of the season, with the exception of large spikes in F_{eb} during a period of rapid decrease in water-table depth when the fields were drained (3-7 August). Again, while both methods capture this spike in F_{eb} , the original method yields substantially larger F_{eb} estimates than the modified method (maximum F_{eb} during drainage spike: 0.33 and 0.16 μ mol m⁻² s⁻¹ based on the original and modified methods, respectively, at the north field; 0.13 and 0.07 μ mol m⁻² s⁻¹ based on the original and modified methods, respectively, at the south field). Seasonal variation in



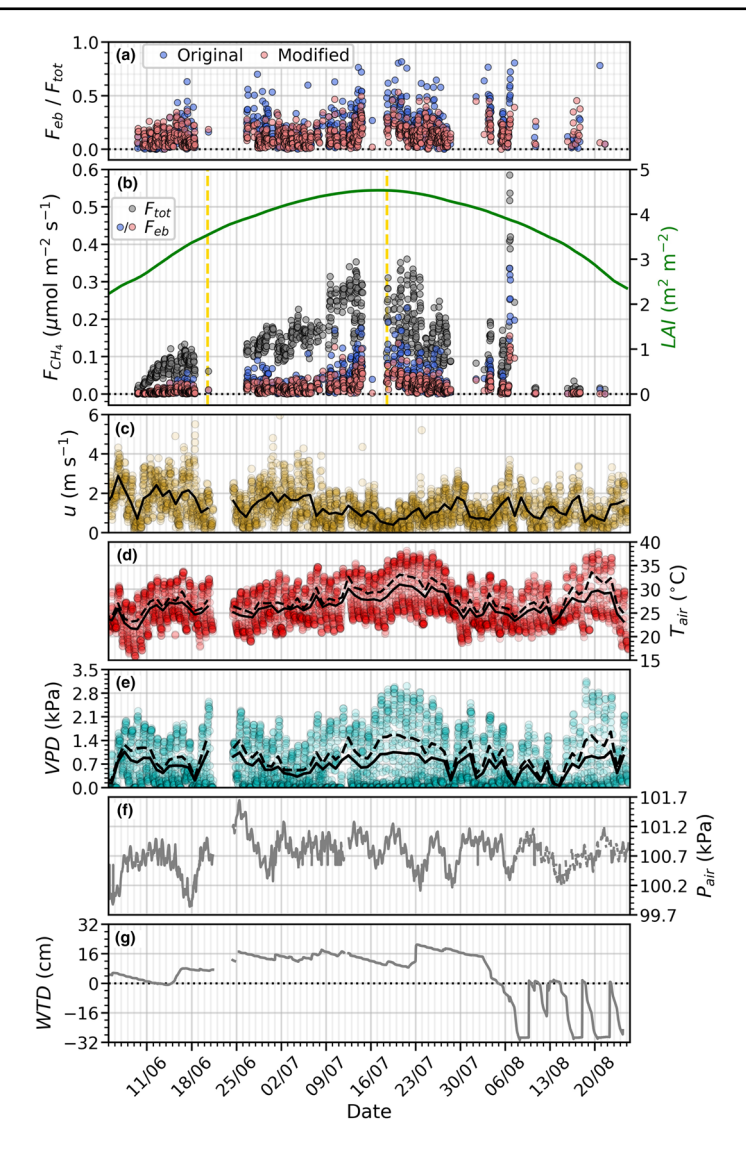


Fig. 8 Time series of partitioned CH₄ fluxes and selected environmental variables at the north field. **a** Fractional ebullition estimates from the original (blue) and modified (pink) partitioning methods (both using the default value for $f_{n,LB}$), **b** total CH₄ fluxes and ebullitive CH₄ fluxes for the corresponding partitioning runs shown in (a) (left y-axis) alongside leaf area index (right y-axis), **c** wind speed, **d** air temperature, **e** vapour pressure deficit, **f** air pressure, and **g** water-table depth. Other than the solid black lines in **c**, **d**, and **e** (daily averages), dashed black lines in **d** and **e** (daily average of daytime observations), and green line in **b** (daily resolution), all data shown are 30-min values. The vertical dashed yellow lines in **b** are approximate delineations of growth stages into vegetative through early reproductive (left), panicle formation through heading (centre), and grain filling and ripening (right); see Sect. 2.6 for more information on growth stage delineations



 F_{eb}/F_{tot} displayed somewhat similar patterns to that of F_{eb} , but the magnitude of F_{eb}/F_{tot} largely remained in the same range across the season (0.0–0.7 based on the original method, 0.0–0.4 based on the modified method; see Fig. 8a and Online Resource 5a), instead showing stronger variation across shorter time scales (i.e., hours to days rather than weeks to months).

Unlike this general similarity in seasonal variation, the two partitioning methods disagreed strongly at the diel time scale (see Fig. 9). Other than from 0900 to 1300 LT the original method yielded higher F_{eb} (and F_{eb}/F_{tot}) than the modified method, and the two methods produced distinctly different patterns of diel variation. For both fields the modified method had lowest F_{eb} during night-time, with fluxes increasing from 1000 LT until a peak between 1400 and 1500 LT (Fig. 9a, b, orange curves). At the north field, F_{eb} based on the original method was lowest in morning hours (0900–1200 LT), increasing to a sustained maximum from afternoon to early evening and followed by a general decrease through night-time hours (Fig. 9a, purple curve). Diel variation in F_{eb} based on the original method at the south field showed less of a clear pattern, oscillating around 0.02 μ mol m⁻² s⁻¹ (Fig. 9b, purple curve). In terms of

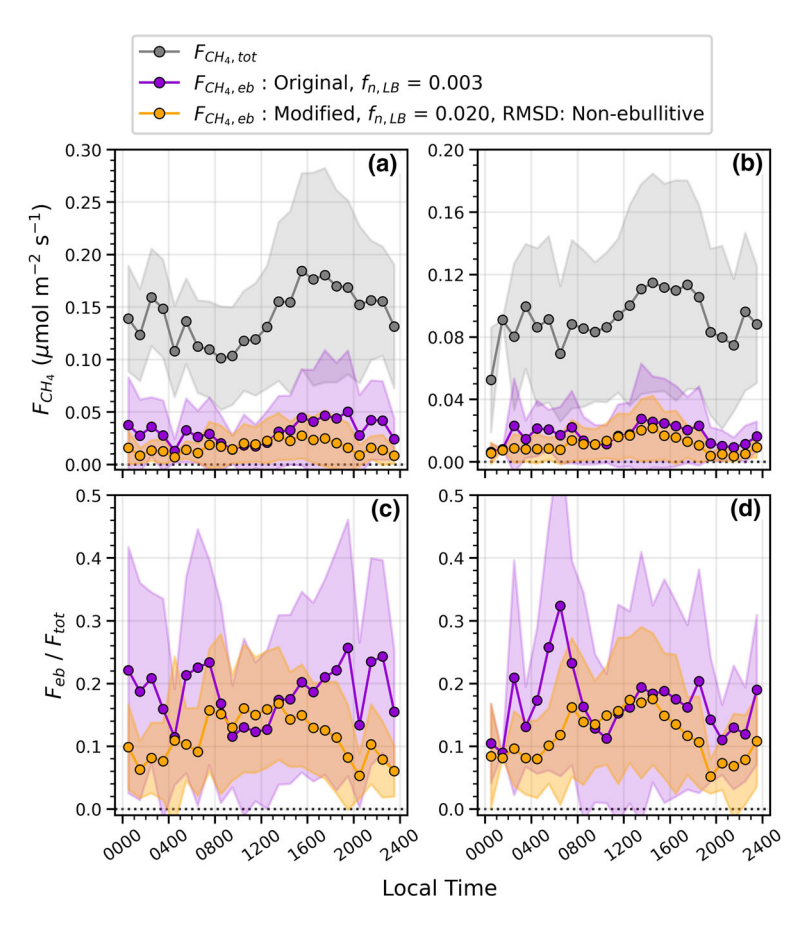


Fig. 9 Diel variation in partitioned CH₄ fluxes (top row) and fractional ebullition (bottom row) for the north (left column) and south (right column) fields across the 2017 growing season. Points show hourly bin averages, and shaded areas encompass \pm 1 standard deviation about the hourly bin averages. Note that $\bf a$ and $\bf b$ have different y-axis limits to enhance visibility of CH₄ fluxes at the south field, which tend to be lower than those at the north field



the relative importance of ebullition across the day, the modified method showed elevated F_{eb}/F_{tot} during midday and afternoon hours (1000–1600 LT) with a maximum hourly bin average of 17% around 1300 LT (Fig. 9c, d, orange curves). Following the elevated afternoon period, F_{eb}/F_{tot} decreased to a minimum of 5% around 2000 LT, increasing slightly over the progression of the night. In stark contrast, the modified method estimated ebullition to be of greatest importance (F_{eb}/F_{tot} as large as 25–32%) during evening and night-time (2000–0030 LT and a spike around 0600 LT at the north field, 0130–0600 LT at the south field) and of least importance during morning and midday hours (Fig. 9c, d, purple curves).

While the original method did not consistently estimate higher F_{eb}/F_{tot} than the modified method on a 30-min basis (data not shown), F_{eb}/F_{tot} based on the original method was significantly higher than that based on the modified method (one-sided t-test, p < 0.01) for both fields when averaged across the growing season (see Table 2, mean values in columns 1 and 2). Considering that the median F_{eb}/F_{tot} between the two methods is more similar, this discrepancy between 30-min and seasonal behaviour highlights the tendency of the original method to produce extreme values. Collectively, the two methods produce distinct magnitudes and dynamics of ebullition whether considering the 30-min, diel, or seasonal time scales.

3.2 Sensitivity Analyses

Increasing $f_{n,LB}$ had the net effect of decreasing the amount of CH₄ flux identified as ebullitive, lowering the mean, median, and IQR of F_{eb}/F_{tot} at both fields (see Table 2, columns 2–5). Mean F_{eb}/F_{tot} decreased by 4.6 percentage points at the north field and 6.3 percentage points at the south field, representing a relative decrease of 35% and 45% across the full range of $f_{n,LB}$, respectively. In other words, lower frequency components of the flux contributed substantially to the estimated ebullitive fluxes if considered in the partitioning. To further characterize sensitivity to the program parameters, we examined variation in F_{eb}/F_{tot} within each 30-min period across the set of partitioning runs used in each sensitivity analysis (hereafter referred to as intra-period variation, see Fig. 10). These distributions of intra-period variation were compared with the distributions of 30-min ebullitive flux random error (see final paragraph of Sect. 2.3.2) normalized by the respective 30-min total flux (yellow distributions, Fig. 10) to provide further context for the magnitude of parameter sensitivity (i.e., is uncertainty due to program parameterization of a similar magnitude to the random error inherent in the flux measurements?). Due to the relatively wide range for $f_{n,LB}$ identified with Fig. 6, we compared both the full range of partitioning runs (blue distributions, Fig. 10a, b) and a reduced range of partitioning runs (red distributions, Fig. 10a, b) to the normalized random error distributions. This comparison gives a sense of how much uncertainty in the resultant F_{eb}/F_{tot} estimates might be mitigated if $f_{n,LB}$ could be more confidently constrained. While narrowing the range of $f_{n,LB}$ did reduce intra-period variation (decrease in median intra-period F_{eb}/F_{tot} standard deviation of 1.0 percentage points for the fields), random error associated with the ebullitive flux estimates was larger than the variation in F_{eb}/F_{tot} due to $f_{n,LB}$ sensitivity (i.e., dotted lines fall to the right of solid lines in Fig. 10a, b).

Similar to the effect of increasing $f_{n,LB}$, widening the ebullition threshold by increasing $RMSD_x$ decreased F_{eb}/F_{tot} (see Table 2, columns 4, 6, 7, 8). Using the smallest $RMSD_x$ value (Table 2, column 6) instead of the baseline $RMSD_x$ (Table 2, column 4) increased mean F_{eb}/F_{tot} by approximately 3.6 percentage points on average for the two fields, representing a relative increase between 35 and 40%. While using the largest $RMSD_x$ value instead of the baseline value decreased mean F_{eb}/F_{tot} by a smaller amount (2.2 percentage points on



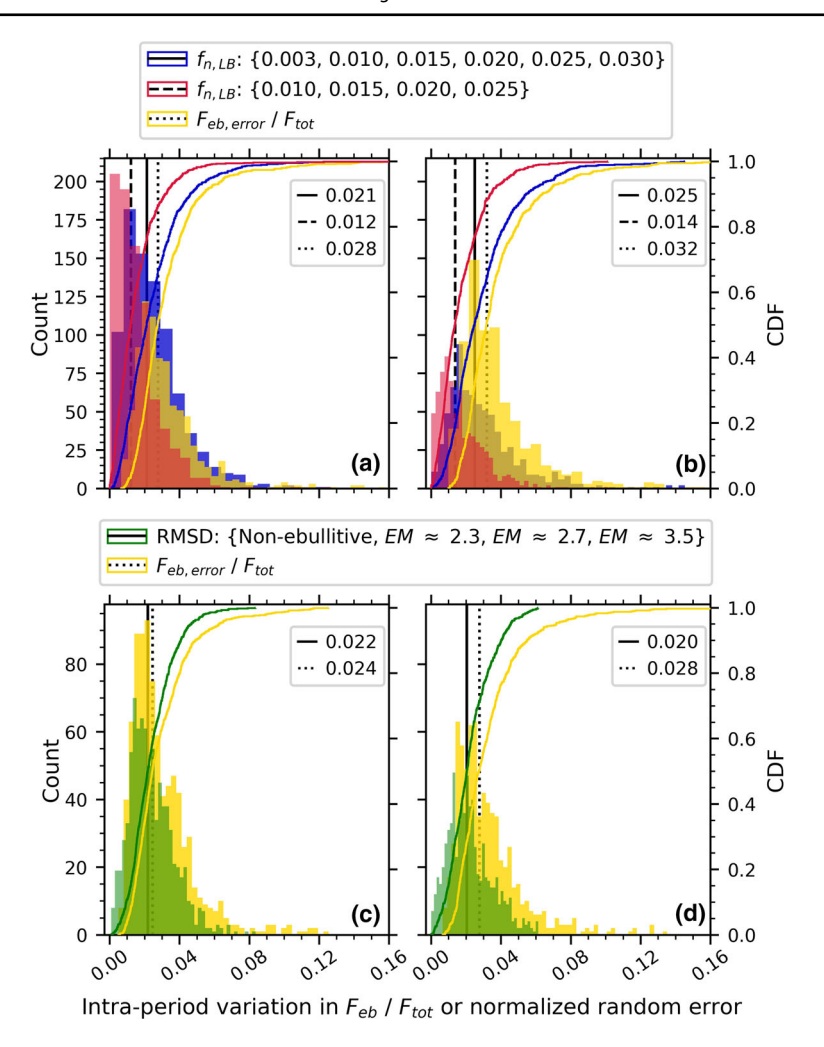


Fig. 10 Sensitivity of partitioning results to changes in $f_{n,LB}$ (top row) and $RMSD_x$ (bottom row) compared with the ebullitive flux normalized random error for the north (left column) and south (right column) fields. Red, blue, and green bars show the distribution of the standard deviation in fractional ebullition within each 30-min period across the partitioning runs in brackets shown in their respective legend entries. Yellow distributions are the mean normalized ebullitive flux random error in each 30-min period across the partitioning runs shown in the blue and green legend entries, respectively. Black lines show the median values of their respective distributions: solid (full ensemble of partitioning runs), dashed (reduced ensemble of partitioning runs, $f_{n,LB}$ only), and dotted (ebullitive flux normalized random error). See Sect. 2.5.2 for more information on the equivalent multiplier (EM) values used in the $RMSD_x$ sensitivity analysis (green legend entry); all partitioning runs used in $RMSD_x$ sensitivity analysis were conducted at $f_{n,LB} = 0.020$

average for the two fields, or a relative decrease of roughly 23%), the largest $RMSD_x$ value was closer to the baseline $RMSD_x$ value than the smallest $RMSD_x$ value (Table 2, column 8). Across the full range of $RMSD_x$ values tested, intra-period variation in F_{eb}/F_{tot} was generally close in magnitude to the normalized ebullitive flux random error (i.e., dotted and solid lines in Fig. 10c, d are close together, especially for the north field). While the results shown in Fig. 10 are in large part based on H_2O as a reference scalar, we also examined the sensitivity



of the partitioning program to its parameters when only using CO_2 as a reference scalar (Online Resource 6). Sensitivity to $f_{n,LB}$ was of a similar magnitude (Online Resource 6a, b as compared with Fig. 10a, b), but partitioning results based on CO_2 were slightly more sensitive to $RMSD_x$ than the harmonized partitioning results (0.1 percentage point increase in median intra-period standard deviation of F_{eb} / F_{tot} for both fields; solid lines in Online Resource 6c, d as compared with those in Fig. 10c, d). Collectively, these results indicate that the magnitudes of ebullition based on the modified partitioning program show non-trivial sensitivity to both $RMSD_x$ and $f_{n,LB}$ and need further constraint to reduce uncertainties in the program outputs. Based on the spectral analysis in Online Resource 1 and relationships shown in Fig. 6, we selected 0.020 as the appropriate $f_{n,LB}$ for these site-years of data. In the absence of further ground-based validation of the method, we decided to leave $RMSD_x$ unchanged from the baseline value for the modified method, resulting in finalized mean F_{eb}/F_{tot} estimates of 10.1% and 8.7% for the north and south fields (Table 2, column 4).

3.3 Biophysical Drivers of Methane Flux Partitioning

Across the ensemble of modified method partitioning runs, correlation coefficients between F_{eb} and predictor variables (as well as between F_{eb}/F_{tot} and predictor variables) showed little variation. The ebullitive flux was most strongly correlated with wind speed (north field r = -0.56, south field r = -0.66; Fig. 11a), R_{eco} (north field r = 0.55, south field r =0.56; Fig. 11b), air temperature (north field r = 0.42, south field r = 0.37), sensible heat flux (north field r = 0.24, south field r = 0.30), and water-table depth (north field r = 0.34, south field r = 0.20). The ration F_{eb}/F_{tot} was most strongly correlated with this same set of variables (most notably with wind speed: north field r = -0.52, south field r = -0.53; Fig. 11c) excluding water-table depth, where correlations were not significant. Partitioning estimates based on the original method generally showed similar patterns of correlation to those based on the modified method, except that correlations with all variables other than wind speed were weaker for the original method (data not shown). Correlations between F_{eb}/F_{tot} and these predictor variables were generally weaker than the respective correlations for F_{eb} , although F_{eb}/F_{tot} had stronger correlations with sensible heat flux (north field r = 0.38, south field r = 0.40; Fig. 11d). While F_{eb} was also significantly correlated with outgoing longwave radiation (north field r = 0.40, south field r = 0.52), four-component net radiation measurements were only sparsely available for the south field, and so these data were excluded from use in further analysis. Thirty-minute change in air pressure had only a weak negative correlation with F_{eb} (north field r = -0.15, south field r = -0.12), while air pressure itself had a positive correlation with F_{eb} that was substantially stronger for the south field (r = 0.36) than the north field (r = 0.20). Interestingly, many of the predictor variables most strongly correlated with F_{tot} were the same variables previously mentioned for F_{eb} : R_{eco} (north field r = 0.68, south field r = 0.64), water-table depth (north field r = 0.68) 0.60, south field r = 0.42), wind speed (north field r = -0.31, south field r = -0.50) and air temperature (north field r = 0.32, south field r = 0.43). As with F_{eb} , F_{tot} was positively correlated with air pressure but more strongly for the south field (r = 0.42) than the north field (r = 0.12). Soil temperature was strongly correlated with F_{tot} for the south field (r = 0.73), but as these data were not available for the north field, we excluded soil temperature from multiple linear regression modelling. While we lacked a complete soil temperature record, the available soil temperature data showed a strong correlation with air temperature (r =0.78).



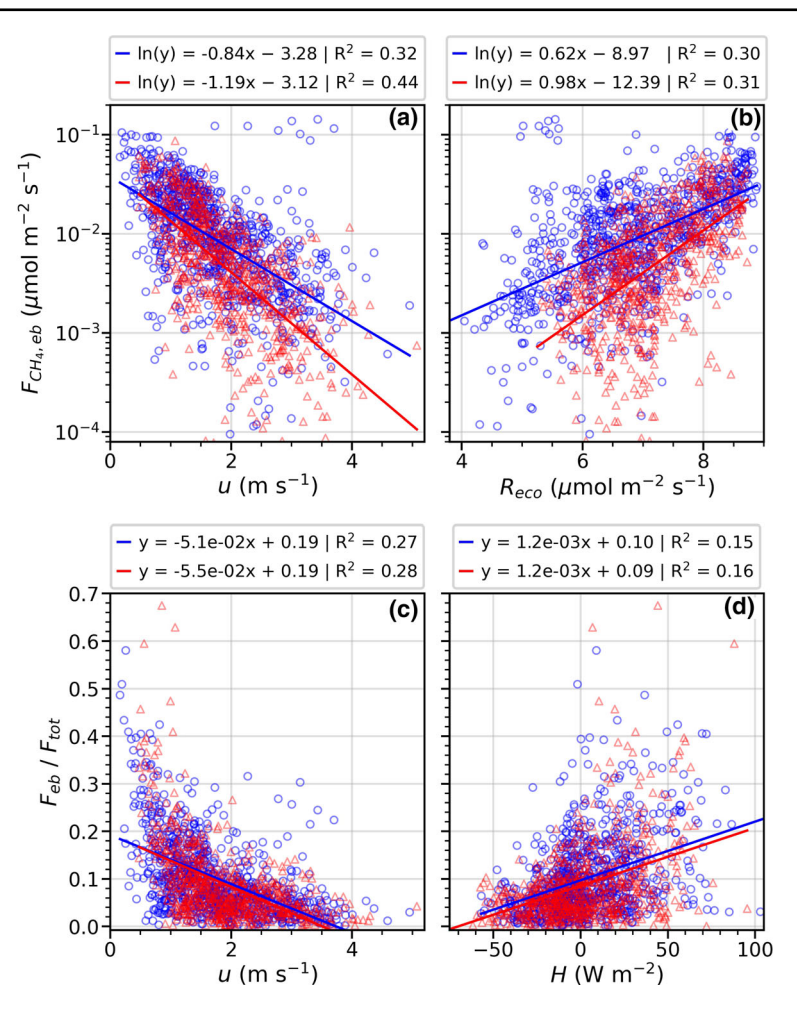
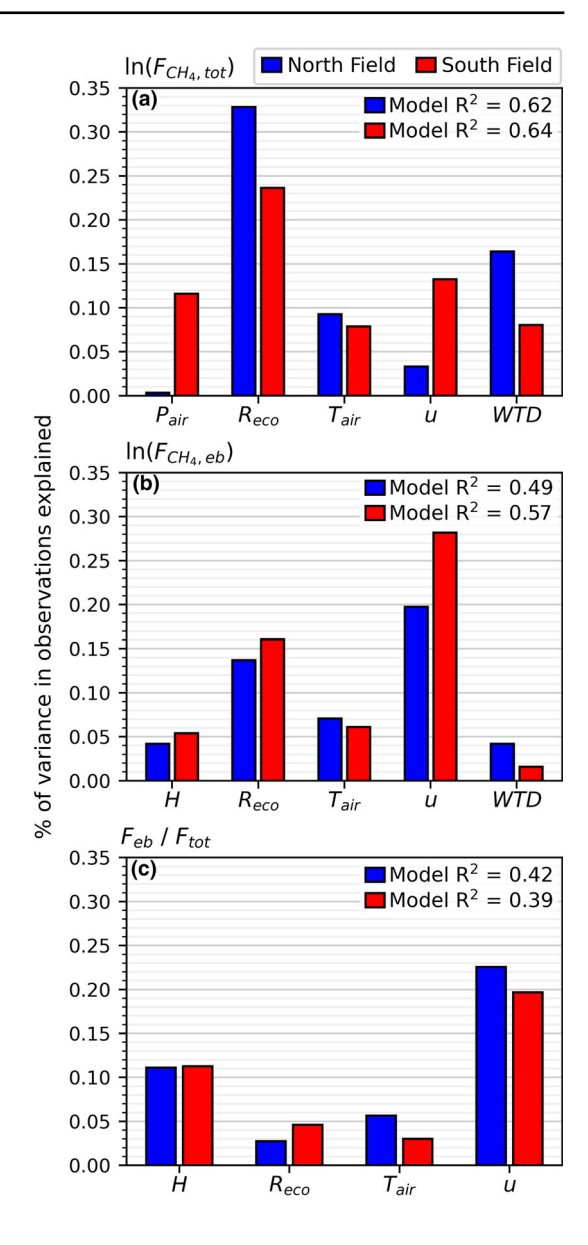


Fig. 11 Scatterplots of log-transformed ebullitive fluxes (top row) and fractional ebullition (bottom row) as a function each quantity's two most informative predictor variables. Predictor variables shown on the *x*-axes are wind speed (**a**, **c**), ecosystem respiration (**b**), and sensible heat flux (**d**). North field data are shown in blue circles (n = 839) and south field data are shown in red triangles (n = 716); the same colour scheme applies to the lines of best fit shown in each plot. The partitioning results displayed are from the modified method with $f_{nLB} = 0.020$, $RMSD_X$ from non-ebullitive periods (i.e., our best estimate)

Final multiple linear regression model R^2 values decomposed into the contributions from each predictor variable are shown in Fig. 12. Models for F_{tot} had better performance ($R^2 = 0.62$; 0.64) than for F_{eb} (0.49; 0.57) and F_{eb}/F_{tot} (0.42; 0.39), with the north field always having the lower R^2 value than the south field, except in the case of F_{eb}/F_{tot} . While both fields shared R_{eco} as the most important predictor variable for F_{tot} (Fig. 12a), wind speed and air pressure were the next most important predictor variables at the south field, whereas water-table depth and air temperature were the next most important predictor variables at the north field. Wind speed and R_{eco} were the most important predictor variables for F_{eb} at both fields (Fig. 12b), although wind speed explained more variance in F_{eb} at the south field than at the north field. While F_{eb}/F_{tot} models had generally poor performance overall, wind speed



Fig. 12 Relative importance of predictor variables in final multiple linear regression models for a log-transformed total CH₄ fluxes, b log-transformed ebullitive CH4 fluxes, and c fractional ebullition at the north and south fields. Red and blue bars show the amount of variance in the response variable that is explained by each predictor variable. See Sect. 2.6 for more information on decomposition of model R^2 values into the unique contribution from each predictor variable. Regression response variable data in b and c are our best partitioning estimates ($f_{n,LB}$ = 0.020, $RMSD_x$ from non-ebullitive periods)



and sensible heat flux were responsible for explaining most of the variance in observations (Fig. 12c).

When split by rice growth stage, the contribution of ebullition to the total flux increased as plants developed (Table 3). Mean F_{eb}/F_{tot} was highest in the grain filling and ripening period (\approx 13%), followed by panicle formation–heading (\approx 8%), and vegetative–early reproductive growth (\approx 6%). Both mean and median F_{eb}/F_{tot} in each growth stage were significantly different from those in the other growth stages (ANOVA and Kruskal–Wallis test, respectively; p < 0.01).



Table 2 Statistics on fractional ebullition estimates (reported as percentages) aggregated across the 2017 growing season for various partitioning runs used in this work

| Site | Statistic (F_{eb}/F_{tot}) | Partitioning Parameters | ameters | | | | | | | |
|-------------|------------------------------|-------------------------|----------|----------|----------|----------|----------|----------|----------|----------|
| | | 77 | Original | Modified |
| | | $f_{n,LB}$ | 0.003 | 0.003 | 0.010 | 0.020 | 0.030 | 0.020 | 0.020 | 0.020 |
| | | $RMSD_x$ type | 0 | × | × | × | × | * | * | * * * |
| North field | Mean | | 18.0 | 13.2 | 12.0 | 10.1 | 9.8 | 13.8 | 11.3 | 7.7 |
| | Median | | 13.6 | 11.4 | 8.6 | 7.5 | 6.2 | 11.3 | 8.8 | 5.4 |
| | SD | | 15.4 | 9.1 | 8.8 | 8.4 | 7.7 | 9.6 | 8.7 | 7.2 |
| | IQR | | 6.7–25.2 | 6.4–17.6 | 5.6–16.4 | 4.1–13.9 | 3.2-11.9 | 7.0–18.6 | 5.2-15.3 | 2.7-10.6 |
| South field | Mean | | 17.2 | 14.0 | 10.8 | 8.7 | 7.7 | 12.2 | 6.6 | 6.7 |
| | Median | | 12.4 | 12.0 | 8.3 | 6.4 | 5.6 | 6.6 | 7.7 | 4.4 |
| | SD | | 16.2 | 6.6 | 8.8 | 8.2 | 9.7 | 9.4 | 9.8 | 7.3 |
| | IQR | | 5.9–23.5 | 7.3–18.5 | 5.1–13.9 | 3.3-10.8 | 2.8-10.1 | 6.1–15.5 | 4.3–12.7 | 2.3–8.7 |
| | | | | | | | | | | |

RMSD_x types '0': mean of *RMSD* in non-ebullitive periods, 'x': mean response of *RMSD-\sigma_m* relationship in non-ebullitive periods, '*: $EM \approx 2.3$ (from quantile regression response of $RMSD-\sigma_m$ relationship in all periods), '**': $EM \approx 2.7$, '***': $EM \approx 3.5$





Table 3 Statistics on fractional ebullition estimates (%) in different rice growth stages. Data shown correspond to the 'finalized' partitioning estimates (modified method, baseline $RMSD_x$, $f_{n,LB} = 0.020$)

| | | Growth stage | | |
|-------------|--------|-------------------------------|---------------------------|----------------------------|
| | | Vegetative–early reproductive | Panicle formation-heading | Grain filling and ripening |
| North field | | (n = 196) | (n = 333) | (n = 310) |
| | Mean | 6.3 | 8.8 | 13.9 |
| | Median | 5.1 | 6.5 | 12.0 |
| | S.D | 5.3 | 7.6 | 9.2 |
| | IQR | 2.6-7.9 | 3.7–11.4 | 7.3–18.5 |
| South field | | (n = 117) | (n = 355) | (n = 244) |
| | Mean | 5.8 | 7.8 | 11.5 |
| | Median | 4.5 | 6.0 | 8.9 |
| | S.D | 4.7 | 6.6 | 10.4 |
| | IQR | 2.4-8.2 | 3.3–9.9 | 5.0-14.3 |

4 Discussion

By thoroughly examining the CH₄ flux partitioning method of Iwata et al. (2018), making subsequent modifications, and conducting a sensitivity analysis on this modified method, we believe we have substantially improved the robustness and applicability of the method. In this section we discuss the implications of our findings for future use of the method, draw inference on the processes controlling ebullition in rice paddies, address uncertainties in our results, and suggest future research opportunities using the method.

4.1 Implications of Method Modifications for Future Implementation

The inclusion of displacement height in the formulation of f_n only had a minor impact on covariance and coherence spectra aggregated across the study period, but this slight shift of the spectra toward lower frequencies prevented further inclusion of low frequency flux components, which may not necessarily maintain scalar similarity in the absence of ebullition (see Online Resource 1). As wetlands globally span a broad range of vegetation types with varying phenology (e.g., the sites included in Delwiche et al. 2021), this modification should make partitioning estimates more robust as the method is applied at more flux tower sites. This consideration is especially important because instruments should be placed relatively close to the surface in order to reliably capture ebullitive signals prior to dilution or mixing (Iwata et al. 2018). While daily canopy height measurements may not be available (or necessary) for some sites, average canopy heights are often reported in flux tower metadata and could be supplemented as necessary with manual or other remote observations (e.g., from PhenoCam imagery), or could be derived as aerodynamic canopy heights from the eddy-covariance data (Chu et al. 2018). Through our exercises with $f_{n,l,B}$ and its sensitivity analysis, we showed that this parameter requires careful scrutiny and can substantially alter partitioning estimates depending on the user's selection (Table 2, Fig. 10a, b). Low frequency components of the CH₄ flux were often classified as ebullitive, likely due to diminished scalar similarity at low



frequencies (e.g., Online Resource 1d, f) even in the absence of ebullition (Ruppert et al. 2006; Foken et al. 2011). Putting f_n values back in the context of wavelet coefficient time scales (Fig. 6) was useful in helping us select a realistic final $f_{n,LB}$ and is recommended for future applications of this method. Furthermore, recent work suggests that the coarser time scale wavelet coefficients should be excluded from scalar similarity-based analyses, as the Haar wavelet has poor time localization at the longest time scales (i.e., lowest frequencies) of the wavelet transform (Zorzetto et al. 2021). Basing wavelet coefficient selection on the integral time scale of vertical velocity fluctuations as in Zorzetto et al. (2021) would provide a useful comparison with the f_n -based approach used in this work.

By conducting the partitioning with multiple reference scalars, we gained important new insights on scalar similarity and its breakdown when flux magnitudes are low. Similar to all previous studies using the partitioning method, H₂O was generally the most reliable reference scalar to use, owing to the large LE at the fields. As most prominent CH₄ emitting sites are frequently inundated, H₂O would likely be the primary reference scalar to use in future applications of the method. The rapid plant growth during agricultural growing seasons is accompanied by large photosynthesis and respiration fluxes, creating conditions for strong CH_4-CO_2 similarity in the absence of ebullition (see Fig. 3f, h). We found that F_{eb}/F_{tot} based on CO₂ largely agreed with the H₂O-based estimate (Online Resource 4), enabling an expanded number of quality ebullition observations (7% increase in the number of best quality 30-min periods for both fields). While the slight disagreements between the reference scalars could indicate a need for slightly higher reference scalar flux thresholds (Fig. 4c, d), this discrepancy cannot be resolved further in the absence of independent ground-based validation of the partitioning method. We suggest instead that it may be useful to take time of day into account when selecting reference scalars. The net CO₂ flux during daytime hours is a mixture of photosynthesis (downward flux) and of respiration (upward flux) while ebullition is an upward release; the resulting mixture of positively and negatively correlated CH₄–CO₂ fluctuations could weaken scalar similarity across a daytime 30-min period. Given that nighttime CO₂ fluxes are solely due to respiration and CH₄-H₂O similarity breaks down most frequently at night due to negligible night-time evapotranspiration, CO₂ may be a more reliable reference scalar than H2O at night (given that respiration fluxes are large enough for scalar similarity with CH₄ to hold). This finding is particularly important considering that it provides an opportunity to expand the observation of ebullition at night, often excluded by chamber measurements (e.g., Minamikawa et al. 2012; Rogers et al. 2013). However, it should be noted that such large CO₂ fluxes may not occur as consistently at natural wetland or lake sites and thus may limit the broader use of CO₂ as a reference scalar. In our initial exploration of the method, we also tried using sonic temperature as a reference scalar but found that the low magnitude sensible heat fluxes at our site made these ebullition estimates generally inconsistent. We note that it may still be worthwhile to pursue sonic temperature as a reference scalar at sites with higher sensible heat fluxes, and this possibility could even be further investigated in our data by isolating periods with the highest sensible heat fluxes.

Of the modifications, the new technique for fitting $RMSD_x$ is likely the most critical departure from the original method, as it changes the ebullition threshold width on a 30-min rather than a monthly time scale. For our site, 30-min RMSD values were strongly driven by σ_m (see Fig. 5), and this relationship was even stronger when only considering the manually identified non-ebullitive periods ($R^2 \ge 0.95$ for both H₂O and CO₂ as reference scalars; red circles in Fig. 5). Furthermore, diel profiles constructed for σ_m showed strong similarity to those of F_{eb}/F_{tot} based on the original method (Online Resource 7e). The strong differences between outputs from the original and modified methods indicate that analyses based on scalar similarity should account for unit magnitudes of the scalars (Hill, 1989), and another



recent wavelet-based CH₄ flux partitioning method (Zorzetto et al. 2021) even normalizes wavelet coefficients by their respective standard deviations prior to assessing scalar similarity. However, as mentioned in Sect. 2.4.3, one drawback of our new $RMSD_x$ fitting technique is that unlike the non-ebullitive periods, the observed σ_m is the result of both ebullitive and diffusive emission. This results in a larger $RMSD_x$ than that based on diffusive W_m alone, thereby reducing the ebullitive flux estimate. One potential solution to this problem would be to iterate the partitioning, using the observed σ_m to fit a first guess for $RMSD_x$. With this initial $RMSD_x$, the user could then calculate a non-ebullitive σ_m using only W_m related to diffusive emission. A new $RMSD_x$ would then be calculated from this non-ebullitive σ_m to partition the flux again, repeating the process until convergence on a value for F_{eb} .

Aside from its utility as a step toward more accurate ebullition estimates, the new $RMSD_x$ fitting technique also eliminates the abrupt month-by-month changes in ebullition threshold width, which may be partially responsible for the sharp decrease in F_{eb}/F_{tot} at the north field based on the original method at the beginning of July (see Fig. 8a). While the $RMSD_x$ values generated via quantile regression were useful for setting up our sensitivity analyses on $RMSD_x$, we recommend continuing the practice of manually identifying non-ebullitive periods for determining $RMSD_x$. This step allows the resultant ebullition thresholds to reliably contain all coefficients showing high scalar similarity, thus enabling the detection of what appeared to be real ebullition for coefficients outside those bounds. Although the partitioning estimates are clearly sensitive to $RMSD_x$ (an $\approx 25\%$ relative decrease in $RMSD_x$ resulted in a 35–40% relative increase in F_{eb} / F_{tot}), the empirical nature of the ebullition threshold width will likely remain unconstrained until future independent validation of the partitioning method (see Sect. 4.3). Further comparison of our $RMSD_x$ sensitivity analysis with that of Iwata et al. (2018) is complicated by (1) the difference in $RMSD_x$ fitting techniques and (2) the reporting of units, as that study reports sensitivity in terms of diffusive flux magnitude, which is of much lower importance for that site (43% of the total flux as reported by Taoka et al. (2020) versus approximately 90% of the total flux at our site).

4.2 Dynamics and Drivers of Ebullition

The average contribution of ebullition to the total flux across the study period, roughly 9% at both fields, is generally consistent with values reported by previous studies in rice paddies (Schütz et al. 1989; Wassmann et al. 1996, 2000; Butterbach-Bahl et al. 1997; Hwang et al. 2020). However, most of these studies reported that the relative importance of ebullition was greatest in early growth stages and decreased with crop development, while we found that F_{eb}/F_{tot} increased over the course of crop development. As the aforementioned studies (excluding Hwang et al. 2020) also had delayed flood irrigation but used static chamber techniques for flux measurement, typical manual measurement protocols (e.g., sampling weekly, Minamikawa et al. 2012) may fail to fully capture the (spatio)temporal variation in rice paddy ebullition. While the modifications made to the original method may be partially responsible for the differences in our observed patterns of F_{eb}/F_{tot} and crop development and those of Hwang et al. (2020), the field in that study was drained for several weeks during the vegetative growth stage in each crop cycle. In that case, nearly all of the preexisting soil CH₄ pool would likely have been released during drainage or subsequently consumed as oxygen entered the soil profile (Denier Van Der Gon et al. 1996). After applying a new flood it would take some time for anaerobic conditions to be re-established (Runkle et al. 2019) and subsequently for gas bubbles to form and accumulate, thus potentially lowering ebullition in later parts of the growing season. Furthermore, early-season land-preparation practices



vary substantially between our study and that of Hwang et al. (2020) due to differences in planting strategy (i.e., drill-seeding versus transplanting). Fields are flooded and then tilled or levelled prior to transplanting (Ge et al. 2018; Bhattacharyya et al. 2019), creating subsurface conditions that could differ from those at our fields. It should be noted that station outages in the early part of this study prevented flux observation during much of the period in which aerenchyma were forming. While we cannot rule out that some substantial ebullitive fluxes occurred during this period, large CH₄ fluxes during the early growing season are more commonly associated with the application of carbon-rich organic fertilizers (Wassmann et al. 1996), and all fertilizers applied to the fields in this study were inorganic.

In addition to this seasonal variation, the modified method provided new insight into dynamics of F_{eb} and F_{eb}/F_{tot} at the diel scale (Fig. 9) and the mechanisms connecting them to their most informative predictor variables (Online Resource 7a-d). A visual comparison of the grey and orange curves in Fig. 9a, b shows that ebullition played some part in shaping the diel cycle of total CH₄ fluxes at the fields, particularly in afternoon hours. Of the relevant predictor variables for F_{eb} (Sect. 3.3, Fig. 12b), R_{eco} and air temperature displayed the most similar diel cycles to F_{eb} (Online Resource 7a, b), suggesting several possible mechanisms driving F_{eb} . Ecosystem respiration was strongly informative of both F_{eb} and F_{tot} (Fig. 12), pointing to a strong connection between microbial activity (i.e., production of new CH₄) and CH₄ emission (Morin et al. 2014; Knox et al. 2016; Irvin et al. 2021), through both the diffusive and ebullitive pathways. Much of the soil CH₄ pool in rice paddy systems consists of gas bubbles, with the proportion of gaseous to total soil CH₄ increasing in later growth stages (Tokida et al. 2013). Thus, the diel synchronization of F_{eb} and temperature may indicate that F_{eb} is driven in part by diel changes in the volume of gas bubbles in the soil resulting from (1) gas expansion and (2) degassing of porewater CH₄ (due to lower solubility) under increased temperature (Green 2013; Tokida et al. 2013). While we found only weak negative relationships between F_{eb} and changes in air pressure at the 30-min scale, air pressure dropped by 0.3 kPa on average during the afternoon period of elevated F_{eb} (Online Resource 7f). This magnitude of air pressure drop has previously been shown to trigger ebullitive fluxes (Mattson and Likens 1990; Tokida et al. 2007; Stanley et al. 2019), so it is possible that air pressure may still be an important driver of ebullition at our fields. More clarity on the relationship between ebullition and air pressure might come through analysis at different time scales, such as considering the change in air pressure over the previous several hours or focusing on synoptic scale change associated with low pressure systems.

Interestingly, the diel cycle of F_{eb}/F_{tot} led that of F_{eb} (particularly at the north field), with the periods of highest importance and daily maxima occurring 1-2 h earlier on average (Fig. 9). Sensible heat flux showed similar patterns of diel variation to F_{eb}/F_{tot} , and portions of the day with elevated F_{eb}/F_{tot} coincided with the largest sensible heat fluxes of the day (Online Resource 7c). As the water surface is largely shaded past a certain point in crop development, positive sensible heat fluxes may be associated with localized sensible cooling at the water surface, causing convective turnover in the water column (Poindexter and Variano 2013). While water column turnover has previously been reported to enhance diffusive emission at sub-daily time scales in wetlands via hydrodynamic transport (e.g., Poindexter et al. 2016), we hypothesize that convective turnover could also enhance ebullitive emission by bringing gas bubbles from the sediment-water interface to the surface (Podgrajsek et al. 2014). Additionally, wind speeds during this time of day were relatively calmer (Online Resource 7d) as compared to the adjacent morning and sunset values; given the relative dominance of diffusive fluxes at our fields, this pattern may indicate that plant-mediated transport is suppressed under lowered wind speeds (i.e., higher wind speeds should promote flushing of CH₄ from the aerenchyma system due to mechanical disturbance of plant stems; Kim



et al. 1999; Wang et al. 2017). Considering that this behaviour occurs at the warmest time of day with highest microbial activity (Online Resource 7a, b), lower plant-mediated transport capacity may indirectly increase F_{eb}/F_{tot} due to an increase in CH₄ accumulation and bubble formation in the soil, as CH₄ production could outpace plant-mediated transport.

4.3 Method Uncertainties and Future Work

The largest source of uncertainty in the ebullitive fluxes from this partitioning method is the lack of validation with independent ebullition observations, which should be a top priority in future work (see below). In the absence of such validation, the random ebullitive flux error generated with the method of Finkelstein and Sims (2001) provided valuable context for potential uncertainty in the partitioning results related to the empirical parameters (Fig. 10). While the magnitude of this uncertainty was generally bounded by the random error inherent in the ebullitive flux estimates, constraining the parameters during validation would further increase confidence in the resultant ebullitive fluxes, as parameter-induced errors could be systematic.

Several other sources of uncertainty remain in the output of the partitioning method. First, although relatively infrequent, F_{eb} estimates were occasionally negative. Bubbling fluxes are positive by definition, so the treatment of these instances (i.e., set to zero or omit from analysis) remains unclear at this point. Negative covariance between the vertical velocity component and CH₄ most commonly occurred in the lower frequency region of the spectrum (Online Resource 1a, b), suggesting that the coarser scale wavelet coefficients may be primarily responsible for negative ebullition estimates. Regardless, more inspection of ebullitive flux cospectra for these periods could provide better understanding of negative scale-wise ebullition, its causes, and its impacts on 30-min F_{eb} estimates. Second, when inspecting high-frequency data during method exploration and development, it was evident that large trends in either CH₄ or the reference scalar tended to produce slightly inflated ebullition estimates. For such periods, it may be useful to run the partitioning program on de-trended time series (e.g., EddyPro Level 7 processed raw data rather than Level 6). Lastly, no spectral corrections are applied to the total flux or its subcomponents by the partitioning program. In our context, the higher frequency components of the flux which are not fully detected by eddy-covariance systems (Moncrieff et al. 1997) are of particular interest. Because the partitioning method is based on observed scalar similarity, applying a spectral correction to the partitioned fluxes would impose an assumption on the relative amount of diffusion and ebullition in the 'missed' CH4 flux. Although the spectral correction on average (1.24) adds a non-negligible amount to F_{tot} , at this time it remains uncertain how a spectral correction would best be applied to the partitioned fluxes.

As previously mentioned, comparison with collocated independent ebullition observations is a crucial next step to validate the partitioning method. Several previous studies have deployed bubble traps or other manual means of measuring ebullition alongside eddy-covariance towers (e.g., McNicol et al. 2017; Männistö et al. 2019; Waldo et al. 2021; Zhao et al. 2021); re-visiting these datasets and applying the partitioning method would be a valuable opportunity to further validate the method without needing to collect more data. However, both in the case of previously collected data and future field campaigns, flux footprint information should be used to isolate periods when the area sampled by the eddy-covariance system overlaps with the locations of manual ebullition sampling. As the method is further validated, it could also be applied at various other lake, wetland, rice, and aquaculture sites, having the potential to greatly improve understanding of CH₄ flux partitioning and our ability



to model CH₄ fluxes. In the future we plan to automate the process of non-ebullitive period selection with a MAD-based screening, investigate an iteration scheme for the partitioning (see Sect. 4.2), and apply the modified partitioning method to more growing seasons of data from these sites, which span a variety of irrigation regimes and environmental conditions. This work should provide opportunities to (1) revisit the contribution of ebullition in early growth stages, (2) focus on the role of ebullition during drainage events, (3) investigate field-to-field differences, and (4) gather more data to inform pathway-specific modeling of rice CH₄ fluxes.

Another useful future research avenue could involve comparing the modified partitioning method with other existing high frequency CH₄ flux processing methods. For example, an intermittent surface renewal method for detecting CH₄ hotspots has recently been developed (Zorzetto et al. 2021) and may provide additional useful comparison with both the original and modified methods. While not focused on ebullition, using other wavelet-based methods for estimating CH₄ fluxes over short time intervals during nonstationary periods (e.g., Schaller et al. 2017) may provide valuable information for improving the partitioning program. The method of Schaller et al. (2017) uses more advanced mother wavelet functions, such as the Mexican hat wavelet, which have better localization in time than the simple Haar wavelet used in our partitioning program. Partitioning CH₄ fluxes using additional mother wavelet functions could be an alternative means of assessing the robustness of our partitioning method. Lastly, it may be interesting to apply the modified method to previous studies using the original method and examine how results change.

5 Conclusion

In this work, we applied and subsequently modified a recently developed CH₄ flux partitioning method in order to accurately quantify ebullitive fluxes from eddy-covariance observations at inundated rice fields. Of the modifications made to the original method, the most critical for robust ebullition detection was scaling the empirical ebullition-threshold parameter $(RMSD_x)$ by the standard deviation of CH₄ concentration measurements. Additionally, we developed new tests to ensure the quality of the partitioning results, namely: using information on the time scales of wavelet coefficients to select the lower frequency bound (Fig. 6) and selecting an appropriate reference scalar for each 30-min period based on reference scalar flux magnitude (Fig. 4c, d). Despite these modifications, this work confirms the observation of Iwata et al. (2018) that ebullition leaves a distinct imprint in the CH₄ concentration data; at this time it remains unclear as to how its detection is impacted by measurement height and mixing length, but making flux observations at multiple measurements may help shed light on the nature of this turbulent exchange (Thomas and Foken 2007). The modified partitioning method produced lower ebullitive fluxes than the original method and revealed coherent diel variation in both ebullitive fluxes and fractional ebullition. We found that ebullition made up approximately 9% of the total CH₄ flux on average, similar to previous studies on rice, although ebullition increased in importance as the crop developed. Sensitivity analyses on the method's empirical parameters showed that the typical intra-period change in fractional ebullition across each parameter's full range was 2-2.5 percentage points (Fig. 10), which was generally less than the amount of random error in the ebullitive flux estimates. Ebullition was enhanced under conditions of low wind speed, high ecosystem respiration, and positive sensible heat flux. Increased application of this method to flux data collected at wetland and



rice sites has great potential to improve understanding of the controls on hot spots or moments of CH₄ emission and further inform process-based CH₄ flux models.

Supplementary Information The online version contains supplementary material available at https://doi.org/10.1007/s10546-022-00703-y.

Acknowledgements This work was funded by the U.S. National Science Foundation CBET division CAREER Award 1752083 and NASA award 80NSSC20K0923 to support Atmospheric Carbon and Transport (ACT)—America, a NASA Earth Venture Suborbital 2 project funded by the NASA Earth Science Division. This research was also supported by the USDA Agricultural Research Service National Program 211. We would like to thank Kosana Suvočarev, Colby Reavis, S. Faye Smith, Yin-Lin Chiu, and Bryant Fong for their assistance with field data collection. We thank the Isbell family and Zero Grade Farms for hosting our team and instrumentation and for managing these fields. Code for the modified partitioning program presented in this study is freely available at https://github.com/richardsonwillp/Wetland-CH4-partition. The datasets generated and analyzed in this study are available from the corresponding author on reasonable request.

References

- Aben RCH, Barros N, Van Donk E, Frenken T, Hilt S, Kazanjian G, Lamers LPM, Peeters ETHM, Roelofs JGM, De Senerpont Domis LN, Stephan S, Velthuis M, Van De Waal DB, Wik M, Thornton BF, Wilkinson J, Delsontro T, Kosten S (2017) Cross continental increase in methane ebullition under climate change. Nat Commun 8:1–8. https://doi.org/10.1038/s41467-017-01535-y
- Baird AJ, Beckwith CW, Waldron S, Waddington JM (2004) Ebullition of methane-containing gas bubbles from near-surface Sphagnum peat. Geophys Res Lett 31:1–4. https://doi.org/10.1029/2004GL021157
- Bhattacharyya P, Dash PK, Swain CK, Padhy SR, Roy KS, Neogi S, Berliner J, Adak T, Pokhare SS, Baig MJ, Mohapatra T (2019) Mechanism of plant mediated methane emission in tropical lowland rice. Sci Total Environ 651:84–92. https://doi.org/10.1016/j.scitotenv.2018.09.141
- De Bruin HAR, Kohsiek W, Van Den Hurk BJJM (1993) A verification of some methods to determine the fluxes of momentum, sensible heat, and water vapour using standard deviation and structure parameter of scalar meteorological quantities. Boundary-Layer Meteorol 63:231–257. https://doi.org/10.1007/BF00710461
- Butterbach-Bahl K, Papen H, Rennenberg H (1997) Impact of gas transport through rice cultivars on methane emission from rice paddy fields. Plant Cell Environ 20:1175–1183. https://doi.org/10.1046/j.1365-3040. 1997.d01-142.x
- Cade BS, Noon BR (2003) A gentle introduction to quantile regression for ecologists. Front Ecol Environ 1:412–420. https://doi.org/10.1890/1540-9295(2003)001[0412:AGITQR]2.0.CO;2
- Christensen TR, Panikov N, Mastepanov M, Joabsson A, Stewart A, Öquist M, Sommerkorn M, Reynaud S, Svensson B (2003) Biotic controls on CO₂ and CH₄ exchange in wetlands a closed environment study. Biogeochemistry 64:337–354. https://doi.org/10.1023/A:1024913730848
- Chu H, Baldocchi DD, Poindexter C, Abraha M, Desai AR, Bohrer G, Arain MA, Griffis T, Blanken PD, O'Halloran TL, Thomas RQ, Zhang Q, Burns SP, Frank JM, Christian D, Brown S, Black TA, Gough CM, Law BE, Lee X, Chen J, Reed DE, Massman WJ, Clark K, Hatfield J, Prueger J, Bracho R, Baker JM, Martin TA (2018) Temporal dynamics of aerodynamic canopy height derived from Eddy covariance momentum flux data across North American flux networks. Geophys Res Lett 45:9275–9287. https://doi.org/10.1029/2018GL079306
- Comas X, Wright W (2012) Heterogeneity of biogenic gas ebullition in subtropical peat soils is revealed using time-lapse cameras. Water Resour Res 48:1–6. https://doi.org/10.1029/2011WR011654
- Delwiche KB, Knox SH, Malhotra A, Fluet-Chouinard E, McNicol G, Feron S, Ouyang Z, Papale D, Trotta C, Canfora E, Cheah Y-W, Christianson D, Alberto MCR, Alekseychik P, Aurela M, Baldocchi D, Bansal S, Billesbach DP, Bohrer G, Bracho R, Buchmann N, Campbell DI, Celis G, Chen J, Chen W, Chu H, Dalmagro HJ, Dengel S, Desai AR, Detto M, Dolman H, Eichelmann E, Euskirchen E, Famulari D, Friborg T, Fuchs K, Goeckede M, Gogo S, Gondwe MJ, Goodrich JP, Gottschalk P, Graham SL, Heimann M, Helbig M, Helfter C, Hemes KS, Hirano T, Hollinger D, Hörtnagl L, Iwata H, Jacotot A, Jansen J, Jurasinski G, Kang M, Kasak K, King J, Klatt J, Koebsch F, Krauss KW, Lai DYF, Mammarella I, Manca G, Marchesini LB, Matthes JH, Maximon T, Merbold L, Mitra B, Morin TH, Nemitz E, Nilsson MB, Niu S, Oechel WC, Oikawa PY, Ono K, Peichl M, Peltola O, Reba ML, Richardson AD, Riley WJ, Runkle BRK, Ryu Y, Sachs T, Sakabe A, Rey-Sanchez AC, Schuur EA, Schäfer KVR, Sonnentag O, Sparks JP, Stuart-Haëntjens E, Sturtevant C, Sullivan RC, Szutu DJ, Thom JE, Torn MS, Tuittila E-S, Turner J, Ueyama M, Valach AC, Vargas R, Varlagin A, Vazquez-Lule A, Verfaillie JG, Vesala T, Vourlitis GL,



- Ward EJ, Wille C, Wohlfahrt G, Wong GX, Zhang Z, Zona D, Windham-Myers L, Poulter B, Jackson RB (2021) FLUXNET-CH₄: A global, multi-ecosystem dataset and analysis of methane seasonality from freshwater wetlands. Earth Syst Sci Data 13:3607–3689. https://doi.org/10.5194/essd-13-3607-2021
- Denier Van Der Gon HAC, Van BN, Neue HU, Lantin RS, Aduna JB, Alberto MCK, Wassmann R (1996) Release of entrapped methane from wetland rice fields upon soil drying. Global Biogeochem Cycles 10:1–7. https://doi.org/10.1029/95GB03460
- Detto M, Katul GG (2007) Simplified expressions for adjusting higher-order turbulent statistics obtained from open path gas analyzers. Boundary-Layer Meteorol 122:205–216. https://doi.org/10.1007/s10546-006-9105-1
- Detto M, Verfaillie J, Anderson F, Xu L, Baldocchi D (2011) Comparing laser-based open- and closed-path gas analyzers to measure methane fluxes using the eddy covariance method. Agric For Meteorol 151:1312–1324. https://doi.org/10.1016/j.agrformet.2011.05.014
- Finkelstein PL, Sims PF (2001) Sampling error in eddy correlation flux measurements. J Geophys Res 106:3503–3509. https://doi.org/10.1029/2000JD900731
- Foken T, Aubinet M, Finnigan JJ, Leclerc MY, Mauder M, Paw U KT (2011) Results of a panel discussion about the energy balance closure correction for trace gases. Bull Am Meteorol Soc 92:ES13–ES18. https://doi.org/10.1175/2011BAMS3130.1
- Foken T, Wichura B (1996) Tools for quality assessment of surface-based flux measurements. Agric For Meteorol 78:83–105. https://doi.org/10.1016/0168-1923(95)02248-1
- Forster PM, Storelvmo T, Armour K, Collins W, Dufresne JL, Frame D, Lunt DJ, Mauritsen T, Palmer MD, Watanabe M, Wild M, Zhang H (2021) The Earth's Energy Budget, Climate Feedbacks, and Climate Sensitivity. In: Masson-Delmotte V, Zhai P, Pirani A, Connors SL, Péan C, Berger S, Caud N, Chen Y, Goldfarb L, Gomis MI, Huang M, Leitzell K, Lonnoy E, Matthews JBR, Maycock TK, Waterfield T, Yelekçi O, Yu R, Zhou B (eds) Climate change 2021: the physical science basis contribution of working group I to the sixth assessment report of the intergovernmental panel on climate change. Cambridge University Press, Cambridge
- Foufoula-Georgiou E, Kumar P (1994) Wavelet analysis in geophysics: an introduction. Academic Press Inc, San Diego
- Gao Z, Bian L, Zhou X (2003) Measurements of turbulent transfer in the near-surface layer over a rice paddy in China. J Geophys Res Atmos 108:1–13. https://doi.org/10.1029/2002jd002779
- Ge HX, Zhang HS, Zhang H, Cai XH, Song Y, Kang L (2018) The characteristics of methane flux from an irrigated rice farm in East China measured using the eddy covariance method. Agric For Meteorol 249:228–238. https://doi.org/10.1016/j.agrformet.2017.11.010
- Green SM (2013) Ebullition of methane from rice paddies: the importance of furthering understanding. Plant Soil 370:31–34. https://doi.org/10.1007/s11104-013-1790-1
- Grömping U (2006) Relative importance for linear regression in R: the package relaimpo. J Stat Softw 17:1–27. https://doi.org/10.18637/jss.v017.i01
- Hill RJ (1989) Implications of Monin-Obukhov similarity theory for scalar quantities. J Atmos Sci 46:2236-2244
- Hoffmann M, Schulz-Hanke M, Garcia Alba J, Jurisch N, Hagemann U, Sachs T, Sommer M, Augustin J (2017) A simple calculation algorithm to separate high-resolution CH₄ flux measurements into ebullition- and diffusion-derived components. Atmos Meas Tech 10:109–118. https://doi.org/10.5194/amt-10-109-2017
- Horst TW, Semmer SR, Maclean G (2015) Correction of a non-orthogonal, three-component sonic anemometer for flow distortion by transducer shadowing. Boundary-Layer Meteorol 155:371–395. https://doi.org/10.1007/s10546-015-0010-3
- Hwang Y, Ryu Y, Huang Y, Kim J, Iwata H, Kang M (2020) Comprehensive assessments of carbon dynamics in an intermittently-irrigated rice paddy. Agric For Meteorol 285–286:107933. https://doi.org/10.1016/ j.agrformet.2020.107933
- Irvin J, Zhou S, McNicol G, Lu F, Liu V, Fluet-Chouinard E, Ouyang Z, Knox SH, Lucas-Moffat A, Trotta C, Papale D, Vitale D, Mammarella I, Alekseychik P, Aurela M, Avati A, Baldocchi D, Bansal S, Bohrer G, Campbell DI, Chen J, Chu H, Dalmagro HJ, Delwiche KB, Desai AR, Euskirchen E, Feron S, Goeckede M, Heimann M, Helbig M, Helfter C, Hemes KS, Hirano T, Iwata H, Jurasinski G, Kalhori A, Kondrich A, Lai DY, Lohila A, Malhotra A, Merbold L, Mitra B, Ng A, Nilsson MB, Noormets A, Peichl M, Rey-Sanchez AC, Richardson AD, Runkle BR, Schäfer KV, Sonnentag O, Stuart-Haëntjens E, Sturtevant C, Ueyama M, Valach AC, Vargas R, Vourlitis GL, Ward EJ, Wong GX, Zona D, Alberto MCR, Billesbach DP, Celis G, Dolman H, Friborg T, Fuchs K, Gogo S, Gondwe MJ, Goodrich JP, Gottschalk P, Hörtnagl L, Jacotot A, Koebsch F, Kasak K, Maier R, Morin TH, Nemitz E, Oechel WC, Oikawa PY, Ono K, Sachs T, Sakabe A, Schuur EA, Shortt R, Sullivan RC, Szutu DJ, Tuittila ES, Varlagin A, Verfaillie JG, Wille C, Windham-Myers L, Poulter B, Jackson RB (2021) Gap-filling eddy covariance methane fluxes:



comparison of machine learning model predictions and uncertainties at FLUXNET-CH4 wetlands. Agric For Meteorol 308–309:108528. https://doi.org/10.1016/j.agrformet.2021.108528

- Iwata H, Hirata R, Takahashi Y, Miyabara Y, Itoh M, Iizuka K (2018) Partitioning eddy-covariance methane fluxes from a shallow lake into diffusive and ebullitive fluxes. Boundary-Layer Meteorol 169:413–428. https://doi.org/10.1007/s10546-018-0383-1
- Kajiura M, Tokida T (2021) Quantifying bubbling emission (ebullition) of methane from a rice paddy using high-time- resolution concentration data obtained during a closed-chamber measurement. J Agric Meteorol 77:245–252. https://doi.org/10.2480/agrmet.D-21-00022
- Katul G, Goltz SM, Hsieh CI, Cheng Y, Mowry F, Sigmon J (1995) Estimation of surface heat and momentum fluxes using the flux-variance method above uniform and non-uniform terrain. Boundary-Layer Meteorol 74:237–260. https://doi.org/10.1007/BF00712120
- Kim J, Verma SB, Billesbach DP (1999) Seasonal variation in methane emission from a temperate Phragmites-dominated marsh: effect of growth stage and plant-mediated transport. Glob Chang Biol 5:433–440. https://doi.org/10.1046/j.1365-2486.1999.00237.x
- Knox SH, Jackson RB, Poulter B, McNicol G, Fluet-Chouinard E, Zhang Z, Hugelius G, Bousquet P, Canadell JG, Saunois M, Papale D, Chu H, Keenan TF, Baldocchi D, Torn MS, Mammarella I, Trotta C, Aurela M, Bohrer G, Campbell DI, Cescatti A, Chamberlain S, Chen J, Chen W, Dengel S, Desai AR, Euskirchen E, Friborg T, Gasbarra D, Goded I, Goeckede M, Heimann M, Helbig M, Hirano T, Hollinger DY, Iwata H, Kang M, Klatt J, Krauss KW, Kutzbach L, Lohila A, Mitra B, Morin TH, Nilsson MB, Niu S, Noormets A, Oechel WC, Peichl M, Peltola O, Reba ML, Richardson AD, Runkle BRK, Ryu Y, Sachs T, Schäfer KVR, Schmid HP, Shurpali N, Sonnentag O, Tang ACI, Ueyama M, Vargas R, Vesala T, Ward EJ, Windham-Myers L, Wohlfahrt G, Zona D (2019) FLUXNET-CH4 synthesis activity: objectives, observations, and future directions. Bull Am Meteorol Soc 100:2607–2632. https://doi.org/10.1175/BAMS-D-18-0268.1
- Knox SH, Matthes JH, Sturtevant C, Oikawa PY, Verfaillie J, Baldocchi D (2016) Biophysical controls on interannual variability in ecosystem-scale CO₂ and CH₄ exchange in a California rice paddy. J Geophys Res Biogeosci 121:978–1001. https://doi.org/10.1002/2015JG003247
- Komiya S, Noborio K, Katano K, Pakoktom T, Siangliw M, Toojinda T (2015) Contribution of ebullition to methane and carbon dioxide emission from water between plant rows in a tropical rice paddy field. Int Sch Res Not 2015:1–8. https://doi.org/10.1155/2015/623901
- Kormann R, Meixner FX (2001) An analytical footprint model for non-neutral stratification. Boundary-Layer Meteorol 99:207–224. https://doi.org/10.1023/A:1018991015119
- Kottek M, Grieser J, Beck C, Rudolf B, Rubel F (2006) World map of the Köppen-Geiger climate classification updated. Meteorol Zeitschrift 15:259–263. https://doi.org/10.1127/0941-2948/2006/0130
- Mallat SG (1989) A theory for multiresolution signal decomposition: the wavelet representation. IEEE Trans Pattern Anal Mach Intell 11:494–513. https://doi.org/10.1109/34.192463
- Mattson MD, Likens GE (1990) Air pressure and methane fluxes. Nature 347:718–719. https://doi.org/10. 1038/347718b0
- Mauder M, Foken T (2015) Documentation and instruction manual of the Eddy-Covariance software package TK3. Zenodo:10.5281/zenodo.20349 https://doi.org/10.5281/zenodo.20349
- McDermitt D, Burba G, Xu L, Anderson T, Komissarov A, Riensche B, Schedlbauer J, Starr G, Zona D, Oechel W, Oberbauer S, Hastings S (2011) A new low-power, open-path instrument for measuring methane flux by eddy covariance. Appl Phys B Lasers Opt 102:391–405. https://doi.org/10.1007/s00340-010-4307-0
- McNicol G, Sturtevant CS, Knox SH, Dronova I, Baldocchi DD, Silver WL (2017) Effects of seasonality, transport pathway, and spatial structure on greenhouse gas fluxes in a restored wetland. Glob Chang Biol 23:2768–2782. https://doi.org/10.1111/gcb.13580
- Le Mer J, Roger P (2001) Production, oxidation, emission and consumption of methane by soils: a review. Eur J Soil Biol 37:25–50. https://doi.org/10.1016/S1164-5563(01)01067-6
- Milliman T, Seyednasrollah B, Young AM, Hufkens K, Friedl MA, Frolking S, Richardson AD, Abraha M, Allen DW, Apple M, Arain MA, Baker J, Baker JM, Bernacchi CJ, Bhattacharjee J, Blanken P, Bosch DD, Boughton R, Boughton EH, Brown RF, Browning DM, Brunsell N, Burns SP, Cavagna M, Chu H, Clark PE, Conrad BJ, Cremonese E, Debinski D, Desai AR, Diaz-Delgado R, Duchesne L, Dunn AL, Eissenstat DM, El-Madany T, Ellum DSS, Ernest SM, Esposito A, Fenstermaker L, Flanagan LB, Forsythe B, Gallagher J, Gianelle D, Griffis T, Groffman P, Gu L, Guillemot J, Halpin M, Hanson PJ, Hemming D, Hove AA, Humphreys ER, Jaimes-Hernandez A, Jaradat AA, Johnson J, Keel E, Kelly VR, Kirchner JW, Kirchner PB, Knapp M, Krassovski M, Langvall O, Lanthier G, Maire G I., Magliulo E, Martin TA, McNeil B, Meyer GA, Migliavacca M, Mohanty BP, Moore CE, Mudd R, Munger JW, Murrell ZE, Nesic Z, Neufeld HS, Oechel W, Oishi AC, Oswald WW, Perkins TD, Reba ML, Rundquist B, Runkle BR, Russell ES, Sadler EJ, Saha A, Saliendra NZ, Schmalbeck L, Schwartz MD, Scott RL, Smith EM, Sonnentag O, Stoy P, Strachan S, Suvočarev K, Thom JE, Thomas RQ, den berg AK, Vargas R, Vogel CS, Walker JJ, Webb N, Wetzel P, Weyers S, Whipple A V, Whitham TG, Wohlfahrt G, Wood



- JD, Yang J, Yang X, Yenni G, Zhang Y, Zhang Q, Zona D, Baldocchi D, Verfaillie J (2019) PhenoCam dataset v2.0: digital camera imagery from the PhenoCam Network, 2000-2018. ORNL DAAC, Oak Ridge, Tennessee, USA. https://doi.org/10.3334/ORNLDAAC/1689
- Minamikawa K, Yagi K, Tokida T, Sander BO, Wassmann R (2012) Appropriate frequency and time of day to measure methane emissions from an irrigated rice paddy in Japan using the manual closed chamber method. Greenh Gas Meas Manag 2:118–128. https://doi.org/10.1080/20430779.2012.729988
- Moncrieff J, Clement R, Finnigan J, Meyers T (2005) Averaging, detrending, and filtering of eddy covariance time series. In: Lee X, Massman W, Law B (eds) Handbook of micrometeorology. Kluwer Academic, London, pp 7–31
- Moncrieff JB, Massheder JM, De Bruin H, Elbers J, Friborg T, Heusinkveld B, Kabat P, Scott S, Soegaard H, Verhoef A (1997) A system to measure surface fluxes of momentum, sensible heat, water vapour and carbon dioxide. J Hydrol 188–189:589–611. https://doi.org/10.1016/S0022-1694(96)03194-0
- Monin AS, Obukhov AM (1954) Basic laws of turbulent mixing in the surface layer of the atmosphere. Tr Geofiz Inst Akad Nauk SSSR 24:163–187
- Monson R, Baldocchi D (2014) Terrestrial biosphere-atmosphere fluxes. Cambridge University Press, New York
- Monteith JL, Unsworth MH (2013) Principles of environmental physics: plants, animals, and the atmosphere. Elsevier, Oxford, UK
- Morin TH, Bohrer G, Frasson RPDM, Naor-Azreli L, Mesi S, Stefanik KC, Schäfer KVR (2014) Environmental drivers of methane fluxes from an urban temperate wetland park. J Geophys Res Biogeosciences 119:2188–2208. https://doi.org/10.1002/2014JG002750
- Männistö E, Korrensalo A, Alekseychik P, Mammarella I, Peltola O, Vesala T, Tuittila ES (2019) Multiyear methane ebullition measurements from water and bare peat surfaces of a patterned boreal bog. Biogeosciences 16:2409–2421. https://doi.org/10.5194/bg-16-2409-2019
- Papale D, Reichstein M, Aubinet M, Canfora E, Bernhofer C, Kutsch W, Longdoz B, Rambal S, Valentini R, Vesala T, Yakir D (2006) Towards a standardized processing of net ecosystem exchange measured with eddy covariance technique: algorithms and uncertainty estimation. Biogeosciences 3:571–583. https://doi.org/10.5194/bg-3-571-2006
- Podgrajsek E, Sahleé E, Rutgersson A (2014) Diurnal cycle of lake methane flux. J Geophys Res Biogeosci 119:236–2481. https://doi.org/10.1002/2013JG002327
- Poindexter CM, Baldocchi DD, Matthes JH, Knox SH, Variano EA (2016) The contribution of an overlooked process to a wetland's methane emissions. Geophys Res Lett 43:6276–6284. https://doi.org/10.1002/ 2016GL068782
- Poindexter CM, Variano EA (2013) Gas exchange in wetlands with emergent vegetation: the effects of wind and thermal convection at the air-water interface. J Geophys Res Biogeosci 118:1297–1306. https://doi.org/10.1002/jgrg.20099
- Reavis CW, Suvočarev K, Reba ML, Runkle BRK (2021) Impacts of alternate wetting and drying and delayed flood rice irrigation on growing season evapotranspiration. J Hydrol 596:126080. https://doi.org/10.1016/ j.jhydrol.2021.126080
- Reichstein M, Falge E, Baldocchi D, Papale D, Aubinet M, Berbigier P, Bernhofer C, Buchmann N, Gilmanov T, Granier A, Grünwald T, Havránková K, Ilvesniemi H, Janous D, Knohl A, Laurila T, Lohila A, Loustau D, Matteucci G, Meyers T, Miglietta F, Ourcival JM, Pumpanen J, Rambal S, Rotenberg E, Sanz M, Tenhunen J, Seufert G, Vaccari F, Vesala T, Yakir D, Valentini R (2005) On the separation of net ecosystem exchange into assimilation and ecosystem respiration: review and improved algorithm. Glob Chang Biol 11:1424–1439. https://doi.org/10.1111/j.1365-2486.2005.001002.x
- Riley WJ, Subin ZM, Lawrence DM, Swenson SC, Torn MS, Meng L, Mahowald NM, Hess P (2011) Barriers to predicting changes in global terrestrial methane fluxes: analyses using CLM4Me, a methane biogeochemistry model integrated in CESM. Biogeosciences 8:1925–1953. https://doi.org/10.5194/bg-8-1925-2011
- Rogers CW, Brye KR, Norman RJ, Gbur EE, Mattice JD, Parkin TB, Roberts TL (2013) Methane emissions from drill-seeded, delayed-flood rice production on a silt-loam soil in Arkansas. J Environ Qual 42:1059–1069. https://doi.org/10.2134/jeq2012.0502
- Runkle BRK, Suvočarev K, Reba ML, Reavis CW, Smith SF, Chiu YL, Fong B (2019) Methane emission reductions from the alternate wetting and drying of rice fields detected using the eddy covariance method. Environ Sci Technol 53:671–681. https://doi.org/10.1021/acs.est.8b05535
- Ruppert J, Thomas C, Foken T (2006) Scalar similarity for relaxed eddy accumulation methods. Boundary-Layer Meteorol 120:39–63. https://doi.org/10.1007/s10546-005-9043-3
- Santoni GW, Lee BH, Goodrich JP, Varner RK, Crill PM, McManus JB, Nelson DD, Zahniser MS, Wofsy SC (2012) Mass fluxes and isofluxes of methane (CH₄) at a New Hampshire fen measured by a continuous



- wave quantum cascade laser spectrometer. J Geophys Res Atmos 117:1–15. https://doi.org/10.1029/2011JD016960
- Saunois M, Stavert AR, Poulter B, Bousquet P, Canadell JG, Jackson RB, Raymond PA, Dlugokencky EJ, Houweling S (2020) The global methane budget 2000–2017. Earth Syst Sci Data 12:1561–1623. https://doi.org/10.5194/essd-12-1561-2020
- Scanlon TM, Albertson JD (2001) Turbulent transport of carbon dioxide and water vapor within a vegetation canopy during unstable conditions: identification of episodes using wavelet analysis. J Geophys Res Atmos 106:7251–7262. https://doi.org/10.1029/2000JD900662
- Schaller C, Göckede M, Foken T (2017) Flux calculation of short turbulent events comparison of three methods. Atmos Meas Tech 10:869–880. https://doi.org/10.5194/amt-10-869-2017
- Schütz H, Seiler W, Conrad R (1989) Processes involved in formation and emission of methane in rice paddies. Biogeochemistry 7:33–53. https://doi.org/10.1007/BF00000896
- Stamp I, Baird AJ, Heppell CM (2013) The importance of ebullition as a mechanism of methane (CH₄) loss to the atmosphere in a northern peatland. Geophys Res Lett 40:2087–2090. https://doi.org/10.1002/grl. 50501
- Stanley KM, Heppell CM, Belyea LR, Baird AJ, Field RH (2019) The importance of CH₄ ebullition in floodplain fens. J Geophys Res Biogeosci 124:1750–1763. https://doi.org/10.1029/2018JG004902
- Suvočarev K, Castellví F, Reba ML, Runkle BRK (2019) Surface renewal measurements of H, λE and CO₂ fluxes over two different agricultural systems. Agric For Meteorol 279:107763. https://doi.org/10.1016/j.agrformet.2019.107763
- Taoka T, Iwata H, Hirata R, Takahashi Y, Miyabara Y, Itoh M (2020) Environmental controls on diffusive and ebullitive methane emission at a sub-daily time scale in the littoral zone of a mid-latitude shallow lake. J Geophys Res Biogeosci. https://doi.org/10.1029/2020JG005753
- Thomas C, Foken T (2007) Flux contribution of coherent structures and its implications for the exchange of energy and matter in a tall spruce canopy. Boundary-Layer Meteorol 123:317–337. https://doi.org/10.1007/s10546-006-9144-7
- Tokida T, Cheng W, Adachi M, Matsunami T, Nakamura H, Okada M, Hasegawa T (2013) The contribution of entrapped gas bubbles to the soil methane pool and their role in methane emission from rice paddy soil in free-air [CO₂] enrichment and soil warming experiments. Plant Soil 364:131–143. https://doi.org/10.1007/s11104-012-1356-7
- Tokida T, Miyazaki T, Mizoguchi M, Nagata O, Takakai F, Kagemoto A, Hatano R (2007) Falling atmospheric pressure as a trigger for methane ebullition from peatland. Global Biogeochem Cycles 21:1–8. https://doi.org/10.1029/2006GB002790
- United Nations Environment Programme and Climate and Clean Air Coalition (2021). Global methane assessment: benefits and costs of mitigating methane emissions. Nairobi: United Nations Environment Programme.
- Vickers D, Mahrt L (1997) Quality control and flux sampling problems for tower and aircraft data. J Atmos Ocean Technol 14:512–526. https://doi.org/10.1175/1520-0426(1997)014%3c0512:QCAFSP% 3e2.0.CO:2
- Villa JA, Ju Y, Yazbeck T, Waldo S, Wrighton KC, Bohrer G (2021) Ebullition dominates methane fluxes from the water surface across different ecohydrological patches in a temperate freshwater marsh at the end of the growing season. Sci Total Environ 767:144498. https://doi.org/10.1016/j.scitotenv.2020.144498
- Virtanen P, Gommers R, Oliphant TE, Haberland M, Reddy T, Cournapeau D, Burovski E, Peterson P, Weckesser W, Bright J, van der Walt SJ, Brett M, Wilson J, Millman KJ, Mayorov N, Nelson ARJ, Jones E, Kern R, Larson E, Carey CJ, Polat İ, Feng Y, Moore EW, VanderPlas J, Laxalde D, Perktold J, Cimrman R, Henriksen I, Quintero EA, Harris CR, Archibald AM, Ribeiro AH, Pedregosa F, van Mulbregt P, Vijaykumar A, Pietro BA, Rothberg A, Hilboll A, Kloeckner A, Scopatz A, Lee A, Rokem A, Woods CN, Fulton C, Masson C, Häggström C, Fitzgerald C, Nicholson DA, Hagen DR, Pasechnik DV, Olivetti E, Martin E, Wieser E, Silva F, Lenders F, Wilhelm F, Young G, Price GA, Ingold GL, Allen GE, Lee GR, Audren H, Probst I, Dietrich JP, Silterra J, Webber JT, Slavič J, Nothman J, Buchner J, Kulick J, Schönberger JL, de Miranda Cardoso JV, Reimer J, Harrington J, Rodríguez JLC, Nunez-Iglesias J, Kuczynski J, Tritz K, Thoma M, Newville M, Kümmerer M, Bolingbroke M, Tartre M, Pak M, Smith NJ, Nowaczyk N, Shebanov N, Pavlyk O, Brodtkorb PA, Lee P, McGibbon RT, Feldbauer R, Lewis S, Tygier S, Sievert S, Vigna S, Peterson S, More S, Pudlik T, Oshima T, Pingel TJ, Robitaille TP, Spura T, Jones TR, Cera T, Leslie T, Zito T, Krauss T, Upadhyay U, Halchenko YO, Vázquez-Baeza Y (2020) SciPy 1.0: fundamental algorithms for scientific computing in Python. Nat Methods 17:261–272. https://doi.org/10.1038/s41592-019-0686-2
- Waldo S, Beaulieu JJ, Barnett W, Balz DA, Vanni MJ, Williamson T, Walker JT (2021) Temporal trends in methane emissions from a small eutrophic reservoir: the key role of a spring burst. Biogeosciences 18:5291–5311. https://doi.org/10.5194/bg-18-5291-2021



- Wang C, Lai DYF, Sardans J, Wang W, Zeng C, Peñuelas J (2017) Factors related with CH₄ and N₂O emissions from a paddy field: clues for management implications. PLoS ONE 12:1–23. https://doi.org/10.1371/journal.pone.0169254
- Wang G, Xia X, Liu S, Zhang L, Zhang S, Wang J, Xi N, Zhang Q (2021) Intense methane ebullition from urban inland waters and its significant contribution to greenhouse gas emissions. Water Res 189:116654. https://doi.org/10.1016/j.watres.2020.116654
- Wassmann R, Aulakh MS (2000) The role of rice plants in regulating mechanisms of methane missions. Biol Fertil Soils 31:20–29. https://doi.org/10.1007/s003740050619
- Wassmann R, Buendia LV, Lantin RS, Bueno CS, Lubigan LA, Umali A, Nocon NN, Javellana AM, Neue HU (2000) Mechanisms of crop management impact on methane emissions from rice fields in Los Baños, Philippines. Nutr Cycl Agroecosyst 58:107–119. https://doi.org/10.1023/A:1009838401699
- Wassmann R, Neue HU, Alberto MCR, Lantin RS, Bueno C, Llenaresas D, Arah JRM, Papen H, Seiler W, Rennenberg H (1996) Fluxes and pools of methane in wetland rice soils with varying organic inputs. Environ Monit Assess 42:163–173. https://doi.org/10.1007/BF00394048
- Webb EK, Pearman GI, Leuning R (1980) Correction of flux measurements for density effects due to heat and water vapour transfer. Q J R Meteorol Soc 106:85–100. https://doi.org/10.1002/qj.49710644707
- Wik M, Crill PM, Varner RK, Bastviken D (2013) Multiyear measurements of ebullitive methane flux from three subarctic lakes. J Geophys Res Biogeosci 118:1307–1321. https://doi.org/10.1002/jgrg.20103
- Wik M, Thornton BF, Bastviken D, Uhlbäck J, Crill PM (2016) Biased sampling of methane release from northern lakes: a problem for extrapolation. Geophys Res Lett 43:1256–1262. https://doi.org/10.1002/ 2015GL066501
- Xu X, Yuan F, Hanson PJ, Wullschleger SD, Thornton PE, Riley WJ, Song X, Graham DE, Song C, Tian H (2016) Reviews and syntheses: four decades of modeling methane cycling in terrestrial ecosystems. Biogeosciences 13:3735–3755. https://doi.org/10.5194/bg-13-3735-2016
- Zhao J, Zhang M, Xiao W, Jia L, Zhang X, Wang J, Zhang Z, Xie Y, Pu Y, Liu S, Feng Z, Lee X (2021) Large methane emission from freshwater aquaculture ponds revealed by long-term eddy covariance observation. Agric For Meteorol 308–309:108600. https://doi.org/10.1016/j.agrformet.2021.108600
- Zorzetto E, Peltola O, Grönholm T, Katul GG (2021) Intermittent surface renewals and methane hotspots in natural peatlands. Boundary-Layer Meteorol 180:407–433. https://doi.org/10.1007/s10546-021-00637-x

Publisher's Note Springer Nature remains neutral with regard to jurisdictional claims in published maps and institutional affiliations.

